Free-space W-band setup for the electrical characterization of materials and mm-wave components

Ó. García-Pérez, F. Tercero, S. López-Ruiz

CDT Technical Report 2017-9

Observatorio de Yebes
Guadalajara (Spain)
E-mail: ogarcia@oan.es

Abstract– This report presents the design, implementation and application of a free-space measurement system operating at W-band (75-110 GHz). The setup consists of two horn antennas connected to a network analyzer, and two dielectric lenses that collimate the beam at the measurement plane. The potential applications are multiple, including characterization of dielectric materials, and measurement of the transmission/reflection parameters of quasioptical components.

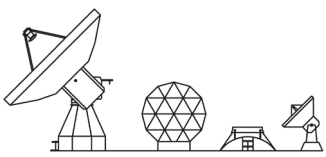

June, 2017

Contents

1 Introduction

1.1 Motivation

The development of increasingly large and complex engineering infrastructures requires precise knowledge of the characteristics of the integrating components and subsystems. Modern radio astronomy antennas are not an exception. Radio waves captured by the parabola are progressively amplified, transformed and processed by different subsystems, and the electrical characterization of each module is of great importance.

In a radio telescope, the incoming signal is redirected and transformed by a series of optical components, such as reflectors, mirrors or lenses. The purpose is to optimally couple the beam to the different feeds at their respective frequencies. At high frequencies, above some tens of GHz, free-space methods allow straightforward characterization of such optical devices. These free-space measurement systems have been extensively proposed to characterize dielectric materials. In radio astronomy, typical examples of dielectric-based components are the membrane in the vertex of the parabola that protects the receiver cabin from the rain, or the vacuum windows in a cryostat housing the cryogenic low-noise amplifiers. Nevertheless, its use is not restricted only to dielectric materials, but can be extended to measure the transmission/reflection response of any planar quasioptical device.

This document presents the design and implementation of a quasioptical test-bench, for free-space characterization of materials and components at W-band (75-110 GHz). This structure allows −in a modular, controlled and stable manner− the assembly, alignment and operation of a high-frequency transmitting/receiving setup. This is of particular interest in the case of free-space propagation, where different parts of the system are not physically connected. A brief description of the dielectric parameters and the different characterization techniques is outlined below. The electrical design of the measurement system, based on the quasioptical theory, is detailed in Section 2. The description of the system assembly, including both mechanical and electrical aspects, as well as the existing methods for free-space calibration, is outlined in

Section 3. The main extraction algorithms used to compute the dielectric properties from the measured scattering (S-) parameters are described in Section 4. Some experimental results to illustrate the functionality of the implemented system are presented in Section 5. Finally, the main conclusions are discussed in Section 6.

1.2 Dielectric materials

The term *dielectric* refers to materials with practically null electrical conductivity. Its electrical behavior is characterized by means of a parameter known as *electrical permittivity* (ε) or *dielectric constant*, which is a measure of how an electric field affects, and is affected by, the dielectric medium. The electrical permittivity is expressed as a complex quantity, in which the real part is related with the energy that can be stored by the material, and the imaginary part is related with its losses.

In practice, the permittivity of a homogeneous material is usually given relative to the vacuum permittivity (i.e., $\varepsilon_0 = 8.85 \cdot 10^{-12}$ F/m), and this normalized parameter is commonly denoted as *relative permittivity*

$$\varepsilon_R = \frac{\varepsilon}{\varepsilon_0} = \varepsilon_R' - j\varepsilon_R''. \tag{1.1}$$

In low-loss materials, the imaginary part (ε_R'') is much lower than the real part (ε_R'). If the complex relative permittivity ε_R is represented as a vector, decomposing the real and imaginary components, the sum vector describes an angle δ with the real axis (Fig. 1.1). Thereby, the ratio between the imaginary part of the permittivity and the real part is defined as *loss tangent*, $\tan(\delta)$ or *dissipation factor*

$$\tan(\delta) = \frac{\varepsilon_R''}{\varepsilon_R'}. \tag{1.2}$$

Just as the electrical permittivity determines the interaction between a material and an electric field, it can be defined a parameter called *magnetic permeability* (μ) to describe the mutual influence between the material and a magnetic field. In the same way, the relative permeability μ_R is determined relative to that in the vacuum (i.e., $\mu_0 = 4\pi \cdot 10^{-7}$ H/m). In our case, most of the materials of interest are non-magnetic and give permeability close to one ($\mu_R \cong 1$), so the analysis will primarily be focused on determining the electrical permittivity.

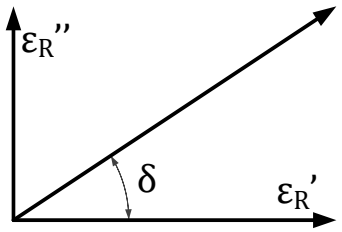

Fig. 1.1: Loss tangent definition.

1.3 Measurement techniques

The experimental characterization of dielectric material properties is usually carried out using indirect methods, analyzing the alterations of the electrical response in a measurement setup when the material-under-test (MUT) is introduced in the system. Therefore, if the theoretical mechanisms in the system are known, it is possible to compare its response with and without the sample, to finally extract its electrical parameters. Following this principle, different techniques have been proposed based on measurements at microwave or millimeter-wave frequencies [1]. They are commonly classified into four groups: coaxial probes, transmission lines, resonant cavities and free-space setups.

1.3.1 Coaxial probes

This method uses the open edge of a coaxial transmission line (probe), which is either immersed into a liquid medium or placed on the surface of a (semi-)solid material [2]. The measured reflection coefficient allows determining the alteration suffered by the fields at the end of the probe due to the presence of the material, and therefore extracting its permittivity. This method is simple, broadband and non-destructive, and is mainly indicated for (lossy) liquids or semi-solids. For solids, the presence of an air gap between the sample and the probe strongly degrades its performance.

1.3.2 Transmission lines

In this case, a sample is placed inside a section of a waveguide or a coaxial transmission line, and the reflection and transmission coefficients are measured [3]. Both the electrical permittivity and magnetic permeability can be extracted in a broad range of frequencies. In general, the sample is machined to present flat faces perpendicular to the line axis, and should fill the whole cross section, avoiding the presence of air gaps at fixture walls.

1.3.3 Resonant cavities

A resonant cavity is a closed structure, which reinforces the fields to form standing waves at a very specific resonant frequency. A piece of material inside the cavity alters both its resonant frequency and the quality factor, which gives information to extract its intrinsic electrical properties [4]. In this case, the measurement is limited to a single frequency, but the method provides improved accuracy with low loss or very thin sheet materials, compared with broadband techniques.

1.3.4 Free space

This setup uses two antennas, faced each other, and a flat slab or sheet of material placed in the middle (Fig. 1.2). The variation of the reflecting and transmitting signals allows determining the electrical permittivity and the magnetic permeability of the

material [5]. Actually, the principle of operation is equivalent to the transmission line, but using free-space signals instead of fields confined in a line. It provides easier characterization at very high frequencies (up to hundreds of GHz), since the sample does not need to be machined to fit the reduced dimensions of a transmission line or a cavity at so high frequencies. Furthermore, the method is broadband and non-contacting. It requires a large, homogeneous, flat and parallel-faced sample. In addition, since the setup is connector-less, it requires an *ad-hoc* free-space calibration kit.

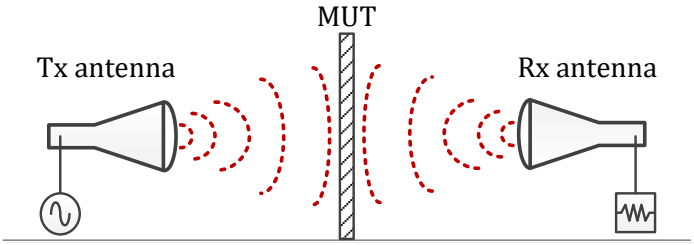

Fig. 1.2: Free-space measurement setup.

Table 1.1: Measurement techniques for dielectric characterization.

Method	Coaxial probe	Transmission line	Resonant cavity	Free space
Features	Broadband, non-destructive	Broadband	Single-frequency, accurate	Broadband, non-contacting
Material assumptions	Semi-infinite thickness, flat surface, best for liquids or semi-solids	Solid sample fills transmission line cross-section, perpendicular flat faces	Small samples, commonly thin sheets or rod-shaped	Large and flat parallel-faced samples
Parameters	s_{11}	s_{11}, s_{21}	Q-factor, f_0	s_{11}, s_{21}
Frequency range (typ.)	0.2 – 50 GHz	50 MHz – 75 GHz	1 – 20 GHz	5 – 500 GHz
Dielectric properties	ε_R	ε_R, μ_R	ε_R, μ_R	ε_R, μ_R

From all the techniques described above, this manuscript presents the development of a general-purpose measurement system based on the free-space technique, with an intended frequency range between 75 and 110 GHz (W band). The choice of the mentioned setup is essentially motivated by:

(a) simpler setup and analysis at high frequencies,
(b) many dielectrics used in radio astronomy systems, such as for the vacuum windows in the cryostats, are already flat slabs, so they can be directly measured in the system (non-destructive),
(c) it can be used for the transmission/reflection characterization of other planar quasioptical components.

2 Quasioptical design

2.1 Quasioptical theory

Quasioptics deals with the propagation of electromagnetic waves whose wavelength is comparable to the size of the optical components, and therefore the effect of diffraction becomes significant. In between conventional optics and microwaves, quasioptics presents a formalism to analyze the propagation of radiation based on Gaussian beam modes, which is of particular interest for the case of mm-wave and THz systems. Some of the main concepts are going to be described below. Nevertheless, an extensive analysis about quasioptical theory and applications can be found in [6].

Let us consider a beam propagating in the positive z direction. For radiation similar to that of a plane wave, but allowing some variation perpendicular to the axis of propagation, a solution for any component of the electric field can be written as

$$E(x, y, z) = u(x, y, z) \exp(-jkz), \tag{2.1}$$

where $k = 2\pi/\lambda$ is the wave number, λ is the wavelength, and u is a complex scalar function that defines the non-plane wave part of the beam.

The scalar field u satisfies the *Helmholtz equation*. In the paraxial approximation, the radiation of the beam is highly collimated, parallel to the axis of propagation, and with some transverse variation. In that case, the Helmholtz equation in rectangular coordinates can be simplified as

$$\frac{\partial^2 u}{\partial x^2} + \frac{\partial^2 u}{\partial y^2} - 2jk\frac{\partial u}{\partial z} = 0, \tag{2.2}$$

which is known as *paraxial wave equation*. Solutions to this equation are the Gaussian beam modes, on which the quasioptical theory is based. These can be expressed in the form of Gauss-Hermite polynomials in rectangular coordinates, or Gauss-Laguerre polynomials in cylindrical coordinates.

Regardless of the system of coordinates, the fundamental mode of the solution to the paraxial wave equation follows a fundamental Gaussian distribution. Let us define $z = 0$ as the location at which the beam radius has its minimum (*beam waist*). The fundamental Gaussian mode can be written as

$$E(r,z) = \frac{A\,\omega_0}{\omega(z)} \cdot \exp\left(-\frac{r^2}{\omega(z)^2}\right) \cdot \exp(-jkz) \cdot \exp\left(-\frac{j\pi r^2}{\lambda R(z)}\right) \cdot \exp\big(j\phi_0(z)\big), \tag{2.3}$$

where r is the distance perpendicular to the axis of propagation, A is a normalization constant, ω is the beam radius, ω_0 is the waist radius, R is the radius of curvature, and ϕ_0 is the Gaussian beam phase shift. Regarding equation (2.3), the first term is for conservation of energy, the second term gives a Gaussian amplitude distribution, the third term is a plane wave delay, the fourth term denotes a spherical wave phase curvature, and the last one is a phase shift term.

The propagation of a Gaussian beam, as well as the relevant beam parameters, is represented in Fig. 2.1. The *beam radius* ω is defined as the half-width value of the beam at which the field falls a factor $1/e$ (-8.7 dB) relative to the on-axis value. The beam radius is a function of z, and its minimum is the *beam waist* ω_0. When a Gaussian beam propagates, the field distribution remains Gaussian, but its beam radius changes as

$$\omega(z) = \omega_0 \sqrt{1 + \left(\frac{z}{z_c}\right)^2}, \tag{2.4}$$

where

$$z_c = \pi\omega_0^2/\lambda, \tag{2.5}$$

is the *confocal distance*, sometimes called *Rayleigh range*, at which the radius of curvature is minimum. The *radius of curvature* also depends on z as

$$R(z) = z\left(1 + \left(\frac{z_c}{z}\right)^2\right). \tag{2.6}$$

The *Gaussian beam phase shift* is defined as

$$\phi_0 = \arctan\left(\frac{z}{z_c}\right). \tag{2.7}$$

In the far-field, that is $z \gg z_c$, the radius of curvature R approximates z, so the beam propagates as a spherical wave. In this case, the beam radius ω grows linearly with z, and the *asymptotic beam growth angle* can be defined as

$$\theta_0 = \tan^{-1}\left(\frac{\lambda}{\pi\omega_0}\right). \tag{2.8}$$

Typically, the beam angle is small and the arctangent can be approximated by its argument.

Quasioptical theory provides a powerful tool for the simple analysis of many radiating systems at mm-wave frequencies. However, some considerations should be addressed:

a) The paraxial approximation performs reasonably well for beam divergence within 30º of the propagation axis. In practice, it is still applied up to 45º, although discrepancies become more significant.
b) Corrugated feed horns provide aperture field distributions extremely similar to a Gaussian function. It means that a fundamental mode analysis is enough to characterize its radiating performance. Other feeds may require multimode analysis, by expanding its aperture field distribution in terms of a set of Gauss-Hermite or Gauss-Laguerre functions. It is still manageable with modern computational tools, but lacks the simplicity of the fundamental mode approach. Consequently, the determinant factor is the fraction of power in the fundamental mode, known as *Gaussicity*, and if it is solely large enough to reasonably represent the radiation pattern. For example, 98% of the power in a corrugated horn is radiated in the fundamental mode, whereas this value reduces to 88% in the case of a rectangular horn.

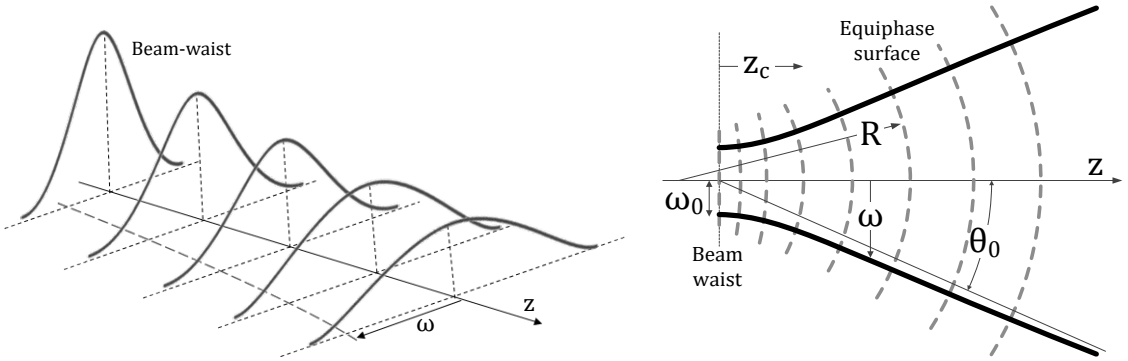

Fig. 2.1: Gaussian beam propagation: (a) electric field sections of a beam propagating from beam waist, and (b) cut showing beam radius and equiphase surfaces along the propagation axis.

2.2 System overview

Due to the intended broadband nature of the system, a *4f* topology has been chosen for the design. This singular configuration is widely used in conventional optics for image processing, and provides an optical path that is frequency-independent [7]. Its scheme is depicted in Fig. 2.2, and is based on two identical lenses separated by twice their focal length f, and the input and output points located at the outer sides, at the

focal points of each lens respectively. Thus, we have a symmetric collinear topology of total length $4f$. Each lens transforms the spherical wave front radiated by the source into a plane wave front at the middle of the system, and vice versa. Since it provides a collimated beam between the two lenses, it can be assumed that a flat sample placed at the middle of the system is illuminated by a plane wave.

With respect to the implementation at mm-wave frequencies, two microwave horn feeds will be used as radiators. Horn antennas provide radiation patterns that can be well characterized by quasioptical theory. Lenses will be manufactured in Teflon, which is an easily available, low loss and low permittivity polymer material. The input beam waist will be located near the aperture of the first horn antenna. The reference plane will be defined at the middle of the system, which coincides with the output beam waist location after the lens, as it is stated by Gaussian optics theory.

The $4f$ topology ideally maximizes power coupling between the two horn antennas. In practice, a fraction of power will be lost due to different causes:

a) reflections, due to impedance mismatching at the horn antennas, and lenses,
b) power dissipated due to dielectric losses of the lens material,
c) beam truncation due to the finite dimensions of the lenses and sample holder,
d) power coupling losses due to imperfect component alignment.

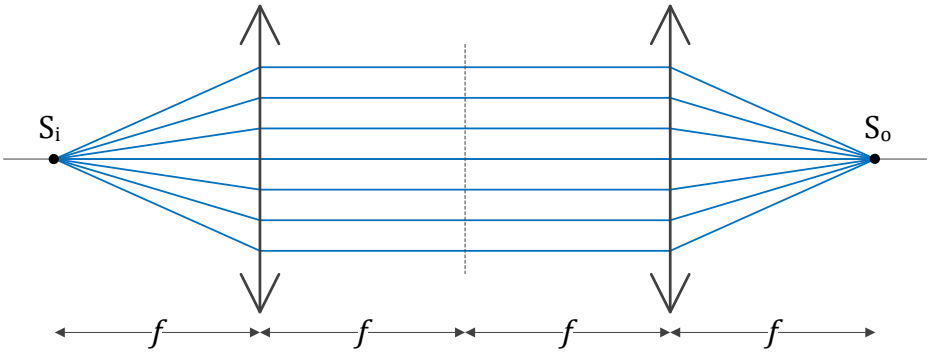

Fig. 2.2: Optical scheme of a *4f* system.

2.3 Rectangular feed horns

There exists a wide variety of commercial feed types and specifications that could meet our system requirements and frequency range. For the present design, standard-gain rectangular horn antennas, model SGH-10 from *Millitech*, have been chosen. The physical dimensions of the antennas are specified in Fig. 2.3. They provide a typical beamwidth of 25º and a typical gain of 24 dB in the band of interest. Although corrugated conical horns provide better Gaussicity, rectangular horns are preferred in

this case due to its broadband behavior, reduced cost, and improved polarization purity.

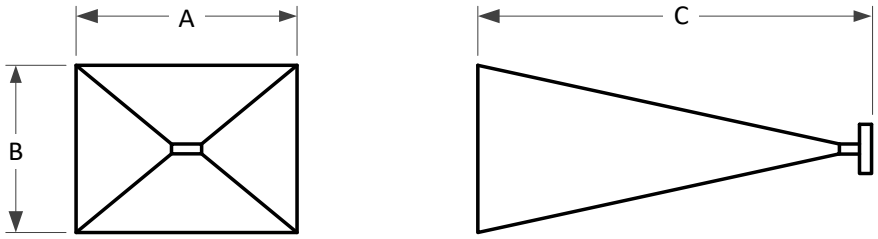

Fig. 2.3: Physical dimensions of the horn feeds: $a = 24.6$ mm, $b = 18.7$ mm, and $c = 49.2$ mm.

The quasioptical analysis of rectangular horns propagating the fundamental TE_{10} mode can be performed by a separate analysis in the two perpendicular coordinates [6]. Larger aperture dimension a will be defined in the x direction, and dimension b in the y direction. At the aperture, the beam radiuses that maximize the coupling to the fundamental Gaussian mode are

$$\omega_x = 0.35a, \qquad \omega_y = 0.5b \tag{2.9}$$

for each coordinate respectively [6]. The beam-waist for a feed horn is not located at its aperture, but at a certain distance z_0 behind it. Both the beam-waist offset and radius can be obtained as

$$z_0 = \frac{R_h}{1 + \left(\lambda R_h / \pi \omega_{x/y}^2\right)^2} \tag{2.10}$$

and

$$\omega_0 = \frac{\omega_{x/y}}{\sqrt{1 + \left(\pi \omega_{x/y}^2 / \lambda R_h\right)^2}}, \tag{2.11}$$

where R_h is the *horn slant length* (see Fig. 2.4). As it can be observed in Fig. 2.5, both parameters present a slight variation with frequency. The beam-waist radius is similar for both coordinates, and can be approximated by $\omega_0 \approx 4.9$ mm. The variation of the waist offset is more critical, since it determines the alignment of the horn with respect to the focal point. Since it cannot be placed at an optimum location for all the frequencies, and moreover it differs in both coordinates, this circumstance will translate into certain loss of coupling efficiency in the system. As a compromise, an offset value of $z_0 \approx 35$ mm will be taken.

The electric field distribution at the aperture of the rectangular horn can be written as

$$E_{ap}(x, y) = \cos\left(\frac{\pi x}{a}\right) \exp\left(-j \frac{\pi (x^2 + y^2)}{\lambda R_h}\right), \tag{2.12}$$

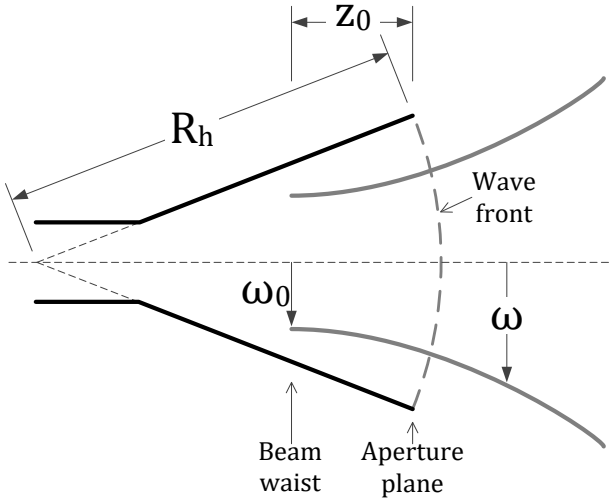

Fig. 2.4: Gaussian beam produced by a feed horn.

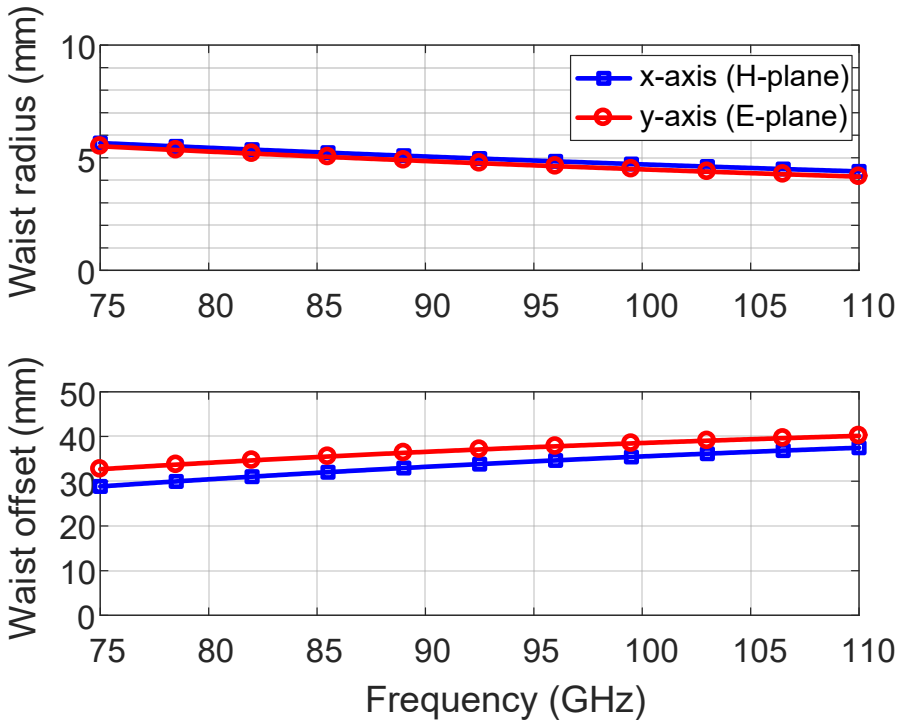

Fig. 2.5: Beam-waist radius ω_0 and beam-waist location z_0 for the rectangular feed horns.

for $|x| \leq a/2$ and $|y| \leq b/2$. The field distribution is separable in both coordinates, so that the quasioptical analysis can be performed separately at x and y directions. In the x direction, the electric field describes a truncated cosine function, which can be efficiently fitted by a simple Gaussian distribution. However, in the y direction the field describes a truncated constant function, which is highly non-Gaussian, and would require Gaussian beam mode expansion to be fitted with some degree of reliability.

Gaussian beam mode expansion consists in decomposing the electric field as

$$E(x,y) = \sum_m \sum_n a_{mn} E_{mn}(x,y), \tag{2.13}$$

where m, n is the order of the mode, and all the E_{mn} form a complete orthonormal system of functions. In Cartesian coordinate system, Gauss-Hermite beam modes are commonly used, so that

$$E_{mn}(x,y) = \frac{1}{\sqrt{\pi\omega_x\omega_y 2^{m+n-1} m!\, n!}} H_m\left(\frac{\sqrt{2}x}{\omega_x}\right) H_n\left(\frac{\sqrt{2}y}{\omega_y}\right) \exp\left(-\frac{x^2}{\omega_x^2} - \frac{y^2}{\omega_y^2} - jkz - \frac{j\pi x^2}{\lambda R_x} - \frac{j\pi y^2}{\lambda R_y} + \frac{j(2m+1)\phi_{0x}}{2} + \frac{j(2n+1)\phi_{0y}}{2}\right), \tag{2.14}$$

where H_m and H_n are Hermite polynomials of order m and n. In the case of the feed aperture, the expansion coefficients a_{mn} can be calculated from the analytical electric field (2.12) as

$$a_{mn} = \iint E_{mn}^*(x,y) E_{ap}(x,y) dxdy. \tag{2.15}$$

It is a good practice to use a normalized version of these coefficients

$$c_{mn} = \frac{a_{mn}}{\sqrt{\mathcal{P}}}, \tag{2.16}$$

where

$$\mathcal{P} = \iint |E(x,y)|^2 dxdy. \tag{2.17}$$

In such a case, the magnitude $|c_{mn}|^2$ represents the fraction of power contained in mode mn. In addition, if the problem is separable in xy coordinates, the mode coefficients can also be decomposed as $c_{mn} = c_{m,x} c_{n,y}$.

The electric field in each coordinate at the horn aperture fitted by a single Gaussian mode, and by the first 50 modes, is represented in Fig. 2.6. The list of computed coefficients is given in Table 2.1. It should be noted that odd Hermite functions are anti-symmetric and, since the aperture field is symmetric in each plane, odd-mode coefficients will be zero. In the x direction, for the truncated cosine function, the fundamental Gaussian mode ($c_{0,x}$) contains 98.9% of power. On the contrary, in the y direction, the fundamental mode ($c_{0,y}$) contains only 89.0% of power, due to the difficulty of representing a truncated constant function by a sum of Gaussian functions (see Fig. 2.6). Accordingly, combining both results, the fundamental Gaussian mode for the two-dimensional expansion (c_{00}) contains 88% of power. In practice, a single fundamental Gaussian beam mode expansion will presumably reproduce well the shape of the main lobe of the beam propagating in the near-field. However, the consideration of the side-lobes, which in this case will be relatively prominent at the E-plane, would require higher-order mode expansion. This will be used for the calculation of the truncation losses at the lens and sample holder.

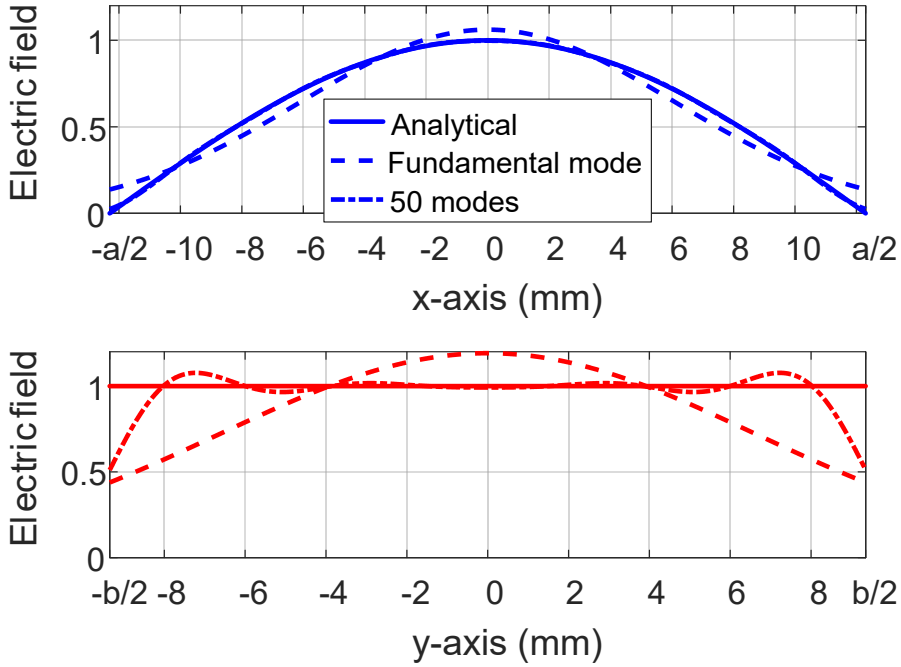

Fig. 2.6: Normalized electric field at the aperture of the feed horn (x, y coordinates), and Gaussian beam mode expansion for a single Gaussian mode and for the first 50 modes.

Table 2.1: Gaussian beam mode expansion of the electric field at the horn aperture.

m/n	$c_{m,x}$	$\sum\lvert c_{m,x}\rvert^2$	$c_{n,y}$	$\sum\lvert c_{n,y}\rvert^2$	$\sum\lvert c_{m,x}\rvert^2 \cdot \sum\lvert c_{n,y}\rvert^2$
0	0.9946	98.93 %	0.9434	89.00 %	88.05 %
2	0.0040	98.93 %	0.0099	89.01 %	88.06 %
4	-0.0895	99.74 %	-0.1812	92.30 %	92.05 %
6	0.0346	99.85 %	0.1464	94.44 %	94.30 %
8	0.0102	99.87 %	-0.0621	94.82 %	94.70 %
10	-0.0238	99.92 %	-0.0126	94.84 %	94.76 %
12	0.0174	99.95 %	0.0589	95.19 %	95.14 %
14	-0.0048	99.95 %	-0.0761	95.76 %	95.72 %
16	-0.0054	99.96 %	0.0706	96.26 %	96.22 %
18	0.0100	99.97 %	-0.0511	96.52 %	96.49 %
20	-0.0095	99.98 %	0.0255	96.59 %	96.57 %
			...		
30	-0.0056	99.986 %	0.0445	97.15 %	97.14 %
			...		
50	0.0007	99.993 %	-0.0302	97.78 %	97.78 %
			...		
100	0.0011	99.998 %	0.0165	98.39 %	98.39 %
			...		
150	-0.0006	99.999 %	0.0077	98.73 %	98.73 %

2.4 Plano-hyperbolic lenses

With regard to the design of the lenses, a first limitation appeared concerning the size of the block of Teflon available for its manufacturing. It restricted the diameter of the lenses to a maximum of $D_l = 180$ mm. In quasioptics, a rule of the thumb to avoid important truncation effects is to design components of dimension $D > 4\omega$, were ω is the beam radius at the aperture. Since the beam propagated by the antenna diverges along its trajectory, there is a maximum focal distance f to place the lens fulfilling the truncation rule. Solving (2.4) for $\omega(z) < D_l/4$, it is determined that the lens should be placed at $f < 193$ mm from the beam waist. For simplicity, it has been chosen a focal number $N = f/D_l$ equals to one, so the focal distance of the system design is $f = 180$ mm. The propagation of the fundamental mode Gaussian beam with these system specifications is illustrated in Fig. 2.7. It can be clearly observed how the radiated field is collimated between the two lenses.

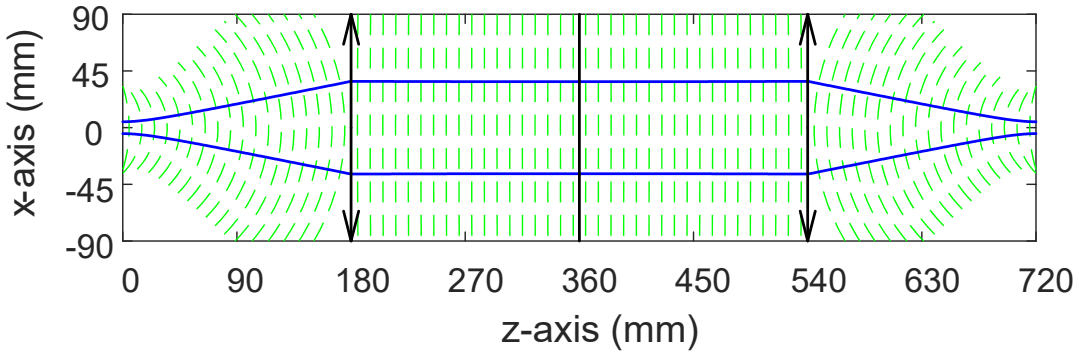

Fig. 2.7: Beam propagation (beam radius in solid-blue, and equiphase curves in dashed-green) along the quasioptical system at 100 GHz.

Since the lens has finite dimensions, the radiated beam will suffer truncation effects. The diameter has been chosen so that $D_l > 4\omega$, which ensures fractional power lost lower than $3 \cdot 10^{-4}$ for the fundamental Gaussian mode [6]. However, as it was seen above, an appreciable amount of power is contained in higher order modes (in particular at E-plane), which means broader main lobe and the presence of significant secondary lobes. Therefore, truncation should be considered in the analysis. To illustrate this effect, the electric field at 100 GHz at the lens interface ($z = f = 180$ mm), reconstructed from the fundamental mode in the x direction (98.9% of power) and 151 modes in the y direction (97.7% of power), is represented in Fig. 2.8. As a reference, the edge of the lens aperture has also been plotted in the graph. Two prominent side lobes appear in the E-plane (y-axis), which are partially truncated by the lens window. The fractional power loss can be evaluated by integrating the radiation pattern that falls inside the aperture. Both the beam radius and the truncation losses at the lens interface are shown in Fig. 2.9. Up to 8.5 % of power is lost due to truncation in the lower part of the band.

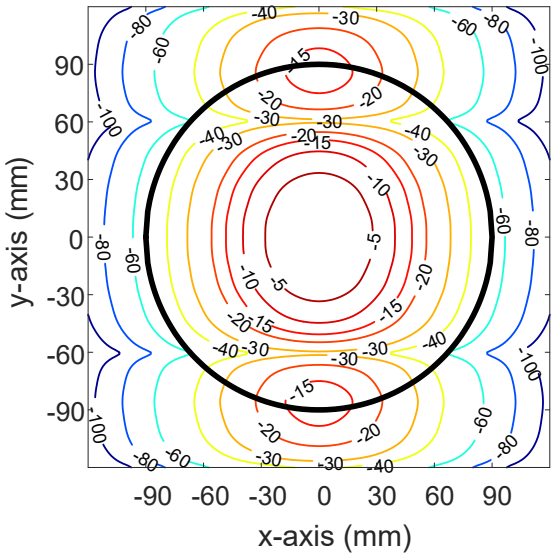

Fig. 2.8: Normalized electric field (dB) of the incident beam (vertical polarization) at the lens interface at 100 GHz, obtained from $c_{0,0}$ to $c_{0,151}$ Gauss-Hermite modes (96.6% of coupled power).

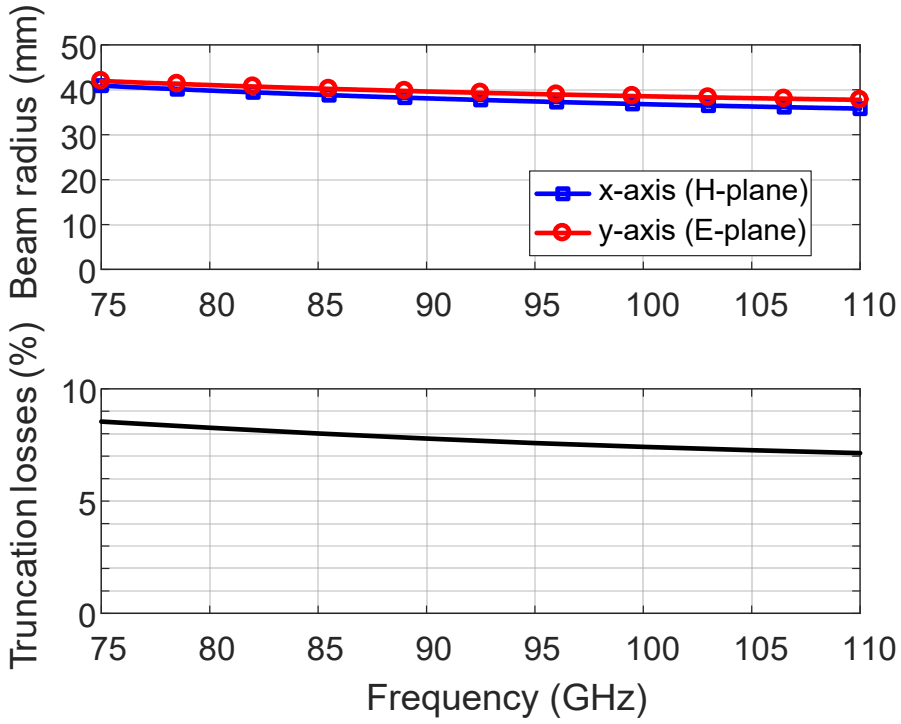

Fig. 2.9: Beam-radius and estimated truncation losses at the lens.

There exist multiple topologies for the design of the lenses. In this case, a plano-hyperbolic design has been chosen, since they are thinner compared with spherical ones, which in turn reduces attenuation losses. The lens will be placed in such a way that none of the surfaces coincides with an equiphase front of the incident wave. In our case, it means that the plane surface is facing the horn feed (quasi-spherical wave front), and the hyperbolic one facing the collimated beam (plane wave front). In this configuration, the power reflected from a surface does not couple back to the incident wave, which avoids the formation of stationary waves and reduces the reflection coefficient seen from the feeds.

Setting the origin of coordinates at the vertex of the hyperbolic face, the curved surface of the lens in cylindrical coordinates can be expressed as [6]

$$r^2 = 2fz(n-1) + z^2(n^2-1), \tag{2.18}$$

whereas the thickness of the lens in a plano-hyperbolic configuration is

$$t_l = \frac{f}{n+1}\left(\sqrt{1+\frac{D_l^2}{4f^2}\frac{(n+1)}{(n-1)}}-1\right), \tag{2.19}$$

which in our design gives $t_l = 40.8$ mm. Reflection and attenuation losses caused by the lens material can be estimated assuming a flat-faced block of Teflon with thickness t_l. Teflon has dielectric constant $\varepsilon_R = 2.05$, index of refraction $n = 1.43$, and loss tangent $\tan(\delta) \approx 5 \cdot 10^{-4}$. Firstly, the reflection parameter obtained from a circuit simulator is shown in the upper plot of Fig. 2.10. Multiple peaks appear in the response due to the in-phase combination of reflected signals at both surfaces of the block at certain frequencies. Peak values of -9.2 dB are obtained, which corresponds to reflection loss of 12 %. Secondly, the signal attenuation due to dielectric losses can be determined as

$$L_d = 1 - \exp\left(-\frac{2\pi n \tan(\delta)}{\lambda_0} t_l\right), \tag{2.20}$$

where λ_0 is the free-space wavelength. As it is observed in the lower plot of Fig. 2.10, this effect is more pronounced at high frequencies, obtaining values as high 6.5 %.

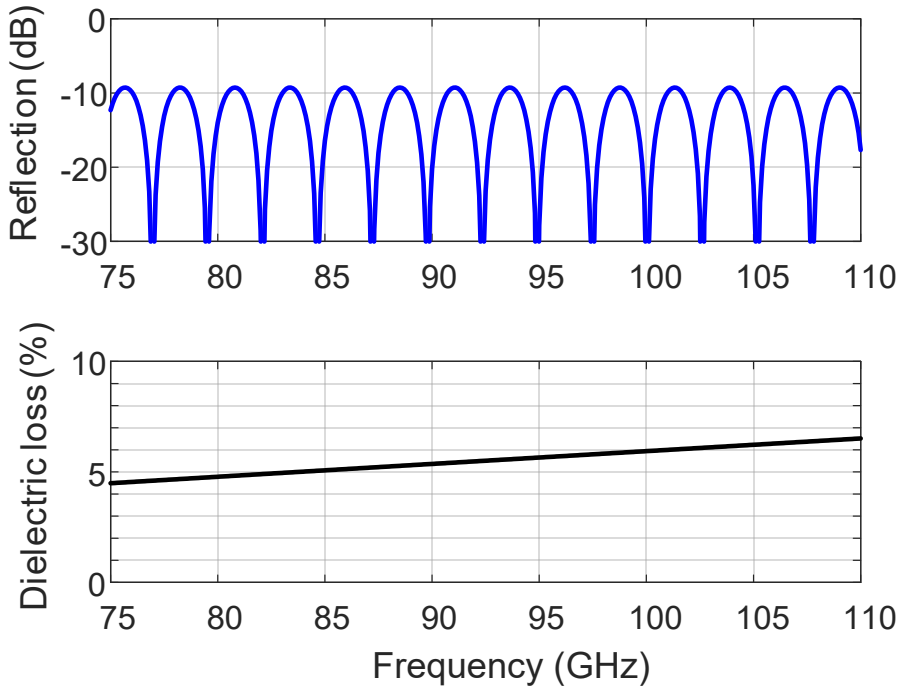

Fig. 2.10: Estimated reflection parameter and dielectric loss of the designed lens made of Teflon.

In practice, lenses usually have thickness that is not negligible (i.e., *thick lenses*). Unlike ideal *thin lenses*, whose focal points are defined with respect to a single plane, two principal planes need to be defined in the case of a thick lens. In general, such planes will not coincide with the position of the two outer vertices. A plane wave coming from one side of the lens will converge at the focal point in the other side. The extended incident and emerged rays meet at points that describe a curved surface, which may o may not reside within the lens. Principal planes, defined in both sides, are the planes that approximate such surfaces in the paraxial region. According to this definition, in the case of a plano-hyperbolic lens one principal plane is tangent to the curved surface, and the other principal plane is located within the lens at a distance h_1, as it is illustrated in Fig. 2.11. Each focal point, F_1 and F_2, is separated a distance f with respect to the corresponding principal plane (which intersect the propagation axis at principal points H_1 and H_2). In the case of the planar surface, principal point H_1 is at a distance denoted as h_1 far from vertex V_1. In the case of the curved surface, principal point H_2 coincides with vertex V_2, and therefore $h_2 = 0$. Distance h_1 can be calculated using the following equation [8]

$$h_1 = -\frac{f(n-1)t_l}{R_2 n}, \tag{2.21}$$

where R_2 is the radius of curvature of the convex surface. The radius of curvature R_2 can be derived from the *Lensmaker's formula* [8]

$$\frac{1}{f} = (n-1)\left(\frac{1}{R_1} - \frac{1}{R_2}\right), \tag{2.22}$$

where $R_1 = \infty$ is the radius of curvature of the planar surface. From (2.22) and (2.21) we obtain that $R_2 = -77.7$ mm (negative means convexity), and $h_1 = 28.5$ mm. This value is important to properly locate the focal point for the feed alignment.

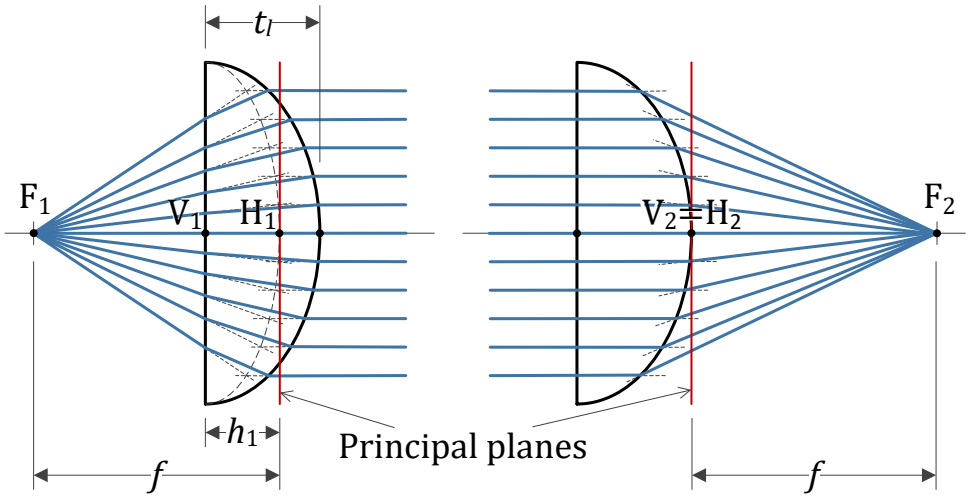

Fig. 2.11: Principal planes in a plano-convex thick lens.

As it was observed in Fig. 2.10, the designed lens made of Teflon and with smooth surfaces may present reflections of about -9.2 dB at certain frequencies. Instead, using rectangular corrugations at the surface may substantially reduce this effect (Fig. 2.12). Such grooved surface, with the appropriate dimensions, acts as a quarter-wave impedance transformer between the lens and the medium. In the case of Teflon ($\varepsilon_R = 2.05$) and air ($\varepsilon_0 = 1$), corrugations should synthesize a layer with permittivity

$$\varepsilon_m = \sqrt{\varepsilon_R \varepsilon_0}\,, \tag{2.23}$$

which in this case corresponds to $\varepsilon_m = 1.43$. The required thickness is

$$d_m = \frac{\lambda_0}{4\sqrt{\varepsilon_m}}, \tag{2.24}$$

which gives $d_m = 0.67$ mm at 92.5 GHz in our case. To avoid higher-order grating effects, the corrugations should be separated [9]

$$2l_g \leq \frac{\lambda_0}{\sqrt{\varepsilon_R}\,(1 + |\sin\theta_r|)}, \tag{2.25}$$

where θ_r is the refracted angle within the lens. Since the half-angle subtended by the lens at the feed is about 36º, the maximum refracted angle obtained from the Snell's law is $\theta_{r,max} \approx 24º$. Applying this to (2.25), we obtain that $2l_g \leq 1.4$ mm at 110 GHz, so a final value of $2l_g = 1.4$ mm has been chosen in this case. The *filling factor* is defined as

$$f_g = \frac{d_g}{l_g}, \tag{2.26}$$

and it has a different optimum value for perpendicular or parallel electric field polarization. In this case, grooves will be cut with rotational symmetry relative to the axis of propagation, so polarization will be spatially dependent with respect to the grooves. In case of random polarization, best performance is obtained for $f_g = 50\,\%$ [10], which implies that $2d_g = 2\,l_g/2 = 0.7$ mm in this case. The main geometrical parameters of the lenses are summarized in Table 2.2.

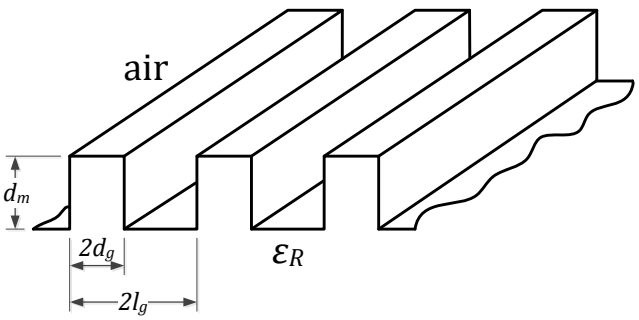

Fig. 2.12: Geometry of a grooved surface.

Table 2.2: Geometrical parameters of the lenses.

Parameter		Value
Material		Teflon
electric permittivity	ε_R	2.05
loss tangent	$\tan(\delta)$	$5{\cdot}10^{-4}$
refraction index	n	1.43
Topology		plano-hyp
Focal distance	f	180 mm
Diameter	D_l	180 mm
Thickness	t_l	40.8 mm
Radius of curvature	R_1	∞
	R_2	-77.7 mm
Distance to principal planes	h_1	28.5 mm
	h_2	0
Corrugations		
depth	d_m	0.67 mm
width	$2d_g$	1.4 mm
separation	$2l_g$	0.7 mm

2.5 Sample holder

The general case in which a Gaussian beam incident to a thin lens is transformed into another Gaussian beam at the output (as it is illustrated in Fig. 2.13) is commonly modeled by means of ABCD matrices. If the input beam waist is located at $d_{in} = f$, the analysis substantially simplifies, since the output beam waist will be located at $d_{out} = f$, and its waist radius can be determined directly as [6]

$$\omega_{0,out} = \frac{\lambda f}{\pi \omega_{0,in}}. \tag{2.27}$$

This is the case of the $4f$ configuration, in which the output beam waist is located at the middle of the system (measurement plane). The radius of curvature of the equiphase surface at the beam waist is infinite, so a sample situated at this point will be illuminated by a collimated plane wave. The calculated output beam waist radius is represented in Fig. 2.14 for the band of interest, and it has an average value of $\omega_{0,out} = 38.4$ mm, which gives an idea about the size of the beam spot with which the sample is illuminated. The dimension of the sample should be chosen in accordance with the size of the beam spot in order to minimize truncation effects. The fractional power transmitted through a sample holder as a function of the diameter of its circular section is also represented in Fig. 2.14. It can be observed that, for 90 % transmission, a sample holder larger than 100 mm is required. If an empty sample holder is used during the calibration process with the network analyzer, truncation effects are, in theory, eliminated from the S-parameter measurement. However, in practice,

truncation reduces the available power at the receivers, and consequently degrades the sensitivity of the RF system.

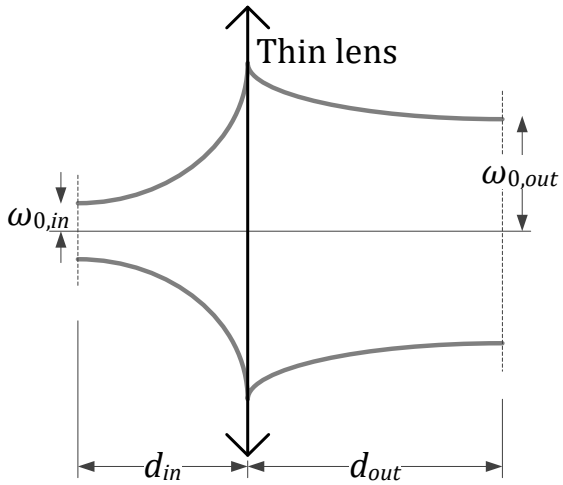

Fig. 2.13: Gaussian beam transformation by a thin lens.

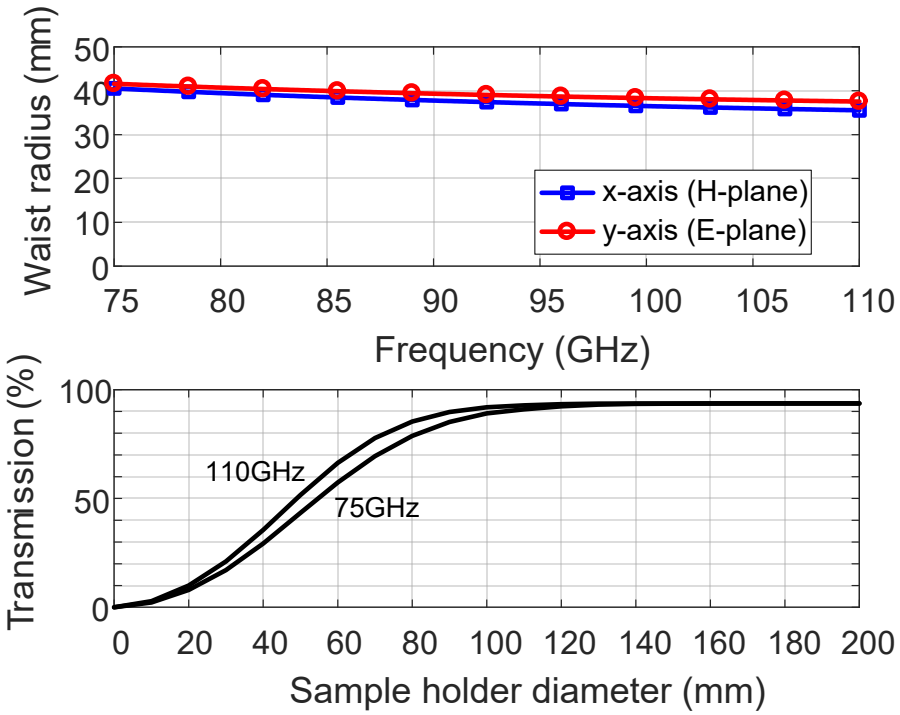

Fig. 2.14: Beam waist radius and estimated truncation losses at the measurement plane.

3 System assembly

3.1 Mechanical and electrical setup

Both the stability and the precision of the system depend to a large extent on an adequate mechanical design. In this case, the system has been mounted on four square aluminum plates (40×40 cm), with a grid of M4 holes separated 50 mm. The plates are joined together by means of longitudinal aluminum bars. A set of sliding rails on the base allows moving the different components longitudinally to its optimal position.

As it was described in Section 2, the system is formed by a transmitter, a receiver, a couple of lenses, and the MUT sample in the middle. In the case of the transmitter/receiver, each mm-wave head is mounted on a platform. The horn feed is held by means of a vertical aluminum plate with a circular hole of the same dimension that the waveguide flange. Such antenna support can be moved forward/backward using the rail mechanism. Each Teflon lens is screwed to an aluminum frame, which can also be moved on the rails. Finally, the sample can be either placed alone or fixed to an aluminum frame. An overview of the system is shown in Fig. 3.1.

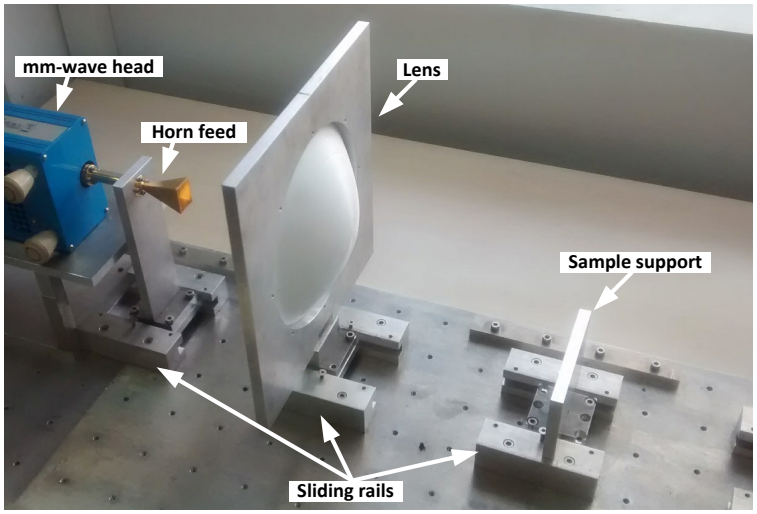

Fig. 3.1: Mechanical design of the implemented system.

The RF setup is represented in Fig. 3.2. The system is formed by a vector network analyzer (*Keysight* PNA 8364B), a mm-wave controller (*Keysight* N5260A), and two mm-wave heads (*OML* WR-10). In few words, the mm-wave heads are transmission/reflection modules with harmonic multipliers, which up/down-convert the signals generated by the VNA. This allows measuring the S-parameters at frequencies well above the maximum frequency of the network analyzer alone (i.e., 50 GHz for the PNA 8364B). In the present configuration, with WR-10 waveguide outputs, the mm-wave signal is in the frequency range of 75-110 GHz. For this band, the RF (radio-frequency) multiplier works at the 6th harmonic and the LO (local oscillator) multiplier at the 8th harmonic [11]. Since the IF (intermediate frequency) signal is at 8.33 MHz, this gives a frequency range for the RF signal of 12.5-18.33 GHz, and the frequency range for the LO signal is 9.38-13.75 GHz.

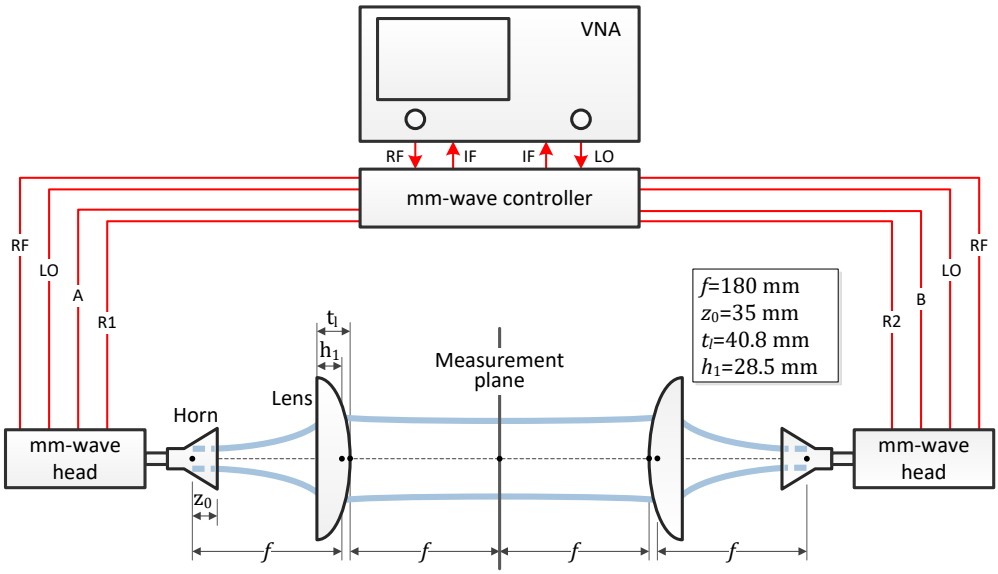

Fig. 3.2: General scheme of the mm-wave measurement system.

3.2 Preliminary tests

Once the system was assembled as indicated in Fig. 3.2, it was appropriate to do some preliminary tests to verify the correct performance of the system. A first test that serves to confirm the correct configuration of the RF equipment, and also to quantify the reflection losses of the horn feeds, consists of measuring the reflection parameter (s_{11}) of such antennas. For this purpose, a waveguide calibration is performed at the interface between the mm-wave heads and the horn antennas. An absorbent material is placed in front of the antenna to avoid undesired external reflections. The measured reflection parameter is shown in Fig. 3.3. It can be observed that this parameter is better than -27 dB in the band of interest, which means return losses lower than 0.2 % in each antenna.

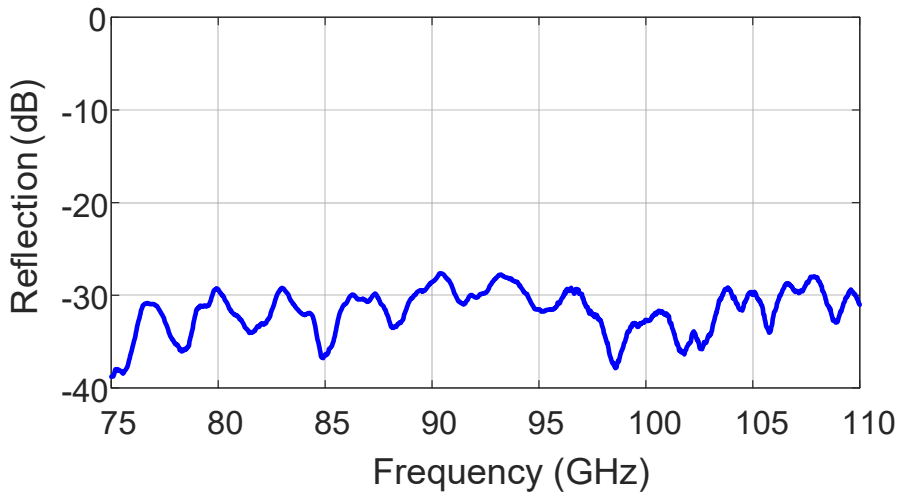

Fig. 3.3: Measured reflection parameter (s_{11}) of the rectangular horn feeds.

The second test consists of measuring the transmission/reflection of the whole system, with no MUT in the middle, and calibrating at the waveguide ends of the mm-wave heads. This setup is particularly useful, since it allows correcting the position of the different components in order to maximize the overall transmitted power. The obtained response is represented in Fig. 3.4. As it can be observed, the transmission parameter varies between -3 and -4 dB in the band of interest, which means that 40-50 % of the power transmitted by the first antenna is effectively received by the other antenna. Main loss contribution comes from the dielectric lenses and their associate losses (truncation, dielectric losses and reflection). Although losses in this kind of free-space lens-based system are appreciably higher than in a transmission-line setup, in which the signal is confined in a closed medium and lossy lenses are not needed, the obtained ratio is enough for S-parameter measurements and dielectric characterization. In practice, system losses are automatically removed from the measured parameters using free-space calibration methods, as it will be explained in the following subsection. A summary with the main contributions in terms of losses, obtained from analysis or measurement, can be found in Table 3.1.

Table 3.1: Main contributions to system losses. Terms (m) and (s) indicate data obtained from measurement or simulation respectively.

		75 GHz		92.5 GHz		110 GHz	
		Loss	Transm.	Loss	Transm.	Loss	Transm.
Horn	Reflection [m]	0.1% (x2)	99.8%	0.2% (x2)	99.6%	0.2% (x2)	99.6%
Lens	Truncation [s]	8.5% (x2)	83.7%	7.8% (x2)	85.0%	7.0% (x2)	86.5%
[*]ungrooved surface.	Reflection [s][*]	12.0% (x2)	77.4%	12.0% (x2)	77.4%	12.0% (x2)	77.4%
	Dissipation [s]	4.5% (x2)	91.2%	5.5% (x2)	89.3%	6.5% (x2)	87.4%
Sample 180 mm	Truncation [s]	5.0%	95.0%	5.0%	95.0%	5.0%	95.0%
TOTAL			56.0%		55.6%		55.4%

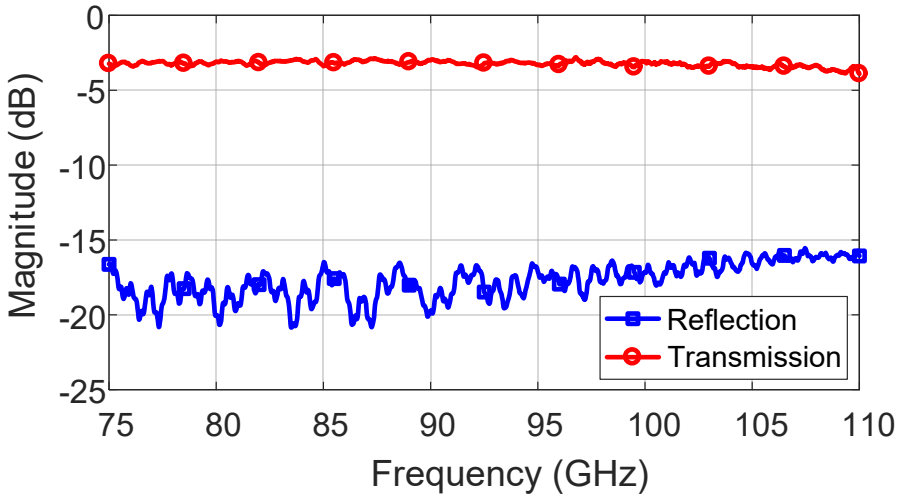

Fig. 3.4: Measured reflection/transmission parameters of the free-space system (thru).

3.3 Free-space calibration methods

In any VNA setup, calibration is required just before a measurement, in order to eliminate the systematic errors of the system. Moreover, it also serves to define the input/output reference planes. In the present setup, the measured parameters need to be referred to both sides of the planar parallel-faced sample, in order to properly calculate the dielectric constant. Calibration methods usable for free-space propagation are in many cases equivalent to those used for guided-wave systems, and they differ in the set of standards that are used. The most common methods for free space are described below.

3.3.1 Thru-reflect-line (TRL)

It requires a high reflection load (*reflect*), and two "transmission lines" of different length (*thru*, *line*). The *reflect* standard can be easily implemented by a metal plate at the center of the system. For the *thru*, the antennas are located at each original positions with the empty sample holder, whereas for the *line* standard one of the antennas should be moved back quarter wavelength, and returned to its original position after calibration. At high frequencies, expensive positioning fixture is required to move the antennas and lenses accurately enough for good calibration (e.g., at 100 GHz, wavelength is only 3 mm). Nevertheless, this method has been extensively used in many free-space systems due to its simplicity, up to frequencies of some GHz [5].

3.3.2 Gated-reflect-line (GRL)

This method has been specifically developed for free-space measurements, and does not need absorbing materials or moving the antennas during calibration. Calibration is performed in two steps. Firstly, a conventional 2-port coaxial or waveguide calibration

is done at the antenna interfaces. Secondly, the free-space calibration is done using *reflect* (metal plate), *line* (thru) and *gated* standards. This third standard is a measurement of the reflection parameter with empty fixture, filtering in the time domain (gating) contributions between the antenna and the measurement plane. Some recent works obtain excellent results using GRL calibration, with improved accuracy with respect to TRL or TRM methods [12]. However, calibration accuracy can be compromised if reflections due to antenna mismatching or any intermediate focusing element are comparable to the power reflected by the *short* [13]. Therefore, this technique may result inappropriate in systems with dielectric lenses.

3.3.3 Thru-reflect-match (TRM)

It uses a zero-length line (*thru*), a high reflection load (*reflect*), and a matched load (*match*). The *match* standard can be synthesized in free-spaced using a piece of absorbent material. The antennas are fixed during calibration, which gives advantage over TRL at very high frequencies. Furthermore, this method is much easier to configure than GRL in a standard VNA. One difficulty can be finding an appropriate broadband absorbing material with enough size. Moreover, imperfections in the match standard cause residual errors after calibration.

Regarding the pros and cons of the calibration methods described above, TRM has been found as preferable for the present free-space setup. The three steps needed for basic TRM calibration are illustrated in Fig. 3.5 (a). In practice, *short* and *match* standards have been respectively implemented by a 0.5 mm-thick aluminum sheet and a 4 cm-thick absorbing block, with dimensions of about 25×25 cm, as it is shown in Fig. 3.5 (b)(c). The *match* standard can be improved if the absorber is tilted about 45º to minimize the reflection towards the ports.

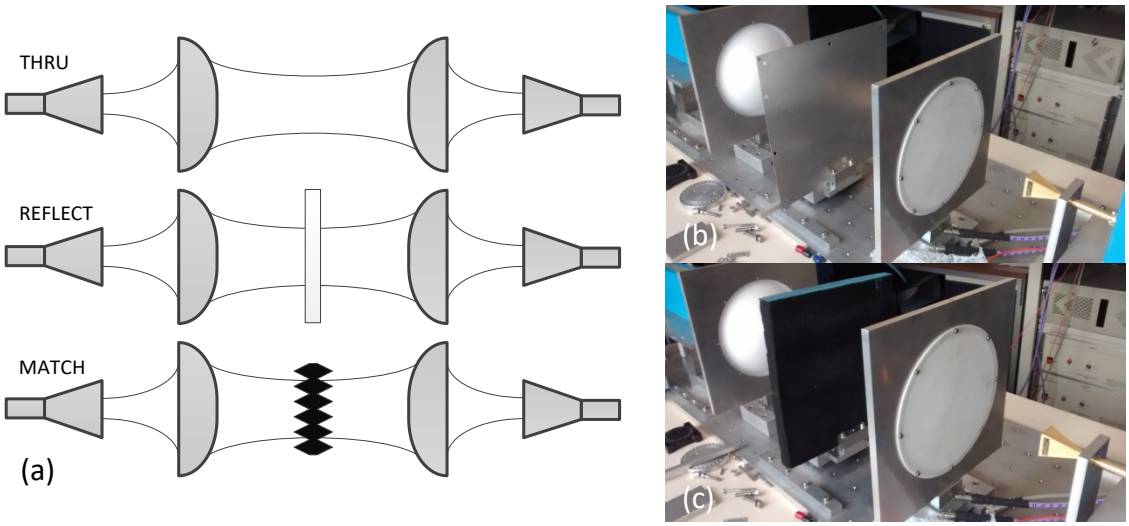

Fig. 3.5: (a) Steps for TRM calibration. Implemented standards *short* (b) and *match* (c).

Conventional TRM calibration would provide a unique reference plane located at the middle of the measurement setup. However, for the correct extraction of the material

properties, the reflection and transmission parameters need to be defined at both faces of the dielectric sample. Therefore, some corrections should be applied to measured 'raw' data [14]:

- Sample misplacement: In practice, the middle plane of the sample could be axially displaced with respect to the center plane of the system (Fig. 3.6). This would cause positive phase shifting in the reflection coefficient at one port, and negative at the other. Since both phase shifts are equal in magnitude, this effect can be easily corrected by computing the resulting phase as the average of the measured phases at both ports.
- Sample thickness: TRM calibration assigns zero value to the phase of the transmission parameter in absence of MUT. In other words, both input and output reference planes coincide, which is valid only for infinitely thin samples (Fig. 3.6). In practice, samples with thickness d are corrected by adding a phase correction factor to the measured reflection and transmission parameters. This factor can be calculated as

$$\phi_d = -\frac{2\pi d}{\lambda_0}, \tag{3.1}$$

  where λ_0 is the free-space wavelength.

- Forbidden phase range: It should be considered that the phase of the reflection coefficient of a dielectric sample cannot take values between -90º and +90º [14]. This can be mathematically corrected by adding an extra 180º factor.

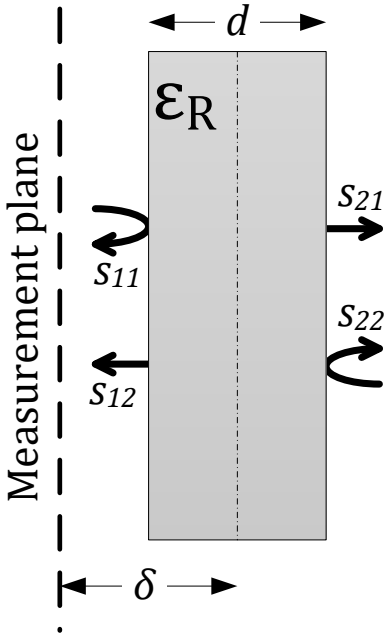

Fig. 3.6: Considerations after TRM calibration: sample misplacement (δ) and sample thickness (d).

In addition to phase corrections, as homogeneous and isotropic samples are usually measured, they can be fully characterized by a pair of reflection/transmission

parameters, so that we can assume $s_{11} = s_{22}$ and $s_{21} = s_{12}$. It is possible to compile all the above corrections into a single set of relations as

$$s_{21} = \left(\frac{|s_{21}^m| + |s_{12}^m|}{2}\right) \cdot \exp\left(j\frac{\angle s_{21}^m + \angle s_{12}^m}{2}\right) \cdot \exp\left(-j\frac{2\pi d}{\lambda_0}\right)$$
$$s_{11} = \underbrace{\left(\frac{|s_{11}^m| + |s_{22}^m|}{2}\right)}_{\text{amplitude averaging}} \cdot \underbrace{\exp\left(j\frac{\angle s_{11}^m + \angle s_{22}^m}{2}\right)}_{\text{phase averaging}} \cdot \underbrace{\exp\left(-j\frac{2\pi d}{\lambda_0}\right)}_{\text{sample thickness}} \cdot \underbrace{\exp\left[j\left(\frac{\pi}{2} \pm \frac{\pi}{2}\right)\right]}_{\text{forbidden phase range}}, \quad (3.2)$$

where the 'raw' S-parameters measured after TRM calibration are denoted as s_{xy}^m, and the corrected parameters as s_{xy}. The module of both parameters is expressed in the first term as the average of measured magnitudes at both VNA ports. The second term is a phase averaging, which in the case of the reflection coefficient serves to correct sample misplacement (δ). The third term is the extra phase term used to consider the sample thickness. Finally, the fourth term in the reflection parameter should be consequently applied to avoid the forbidden -90º to +90º phase range. Apart from the previous corrections, smoothing can be applied to measured data in the VNA to reduce jitter effects.

4 Extraction algorithms

Obtaining the intrinsic properties of a dielectric material from the measurement of the S parameters (either in a guided or free-space setup) is not trivial, since we have to solve a system of equations that is overdetermined due to phase ambiguities. In order to overcome this circumstance, multiple algorithms have been developed to extract the dielectric parameters.

4.1 Nicolson-Ross-Weir (NRW)

This model was originally developed by A. M. Nicolson and G. F. Ross for time domain [3], and later adapted by W. W. Weir for frequency domain using a network analyzer [15]. The algorithm is fast and non-iterative, and it allows extracting both the magnetic permeability μ_R and the electric permittivity ε_R of a material from the reflection and transmission measurements of the sample. However, it is inaccurate for low-loss materials, and diverges when the thickness of the sample is multiple of half-wavelength.

The S-parameters of a dielectric slab can be written as [3]

$$s_{11} = \frac{\Gamma(1-T^2)}{1-\Gamma^2 T^2}, \qquad s_{21} = \frac{T(1-\Gamma^2)}{1-\Gamma^2 T^2}, \tag{4.1}$$

where Γ is the reflection at the interface of a semi-infinite sample, and T is the transmission coefficient between both faces in a sample of a given thickness d. The reflection coefficient Γ can be derived in terms of S-parameters as [15]

$$\Gamma = X \pm \sqrt{X^2 - 1}, \tag{4.2}$$

being $|\Gamma| < 1$, and where

$$X = \frac{s_{11}^2 - s_{21}^2 + 1}{2s_{11}}. \tag{4.3}$$

On the other hand, the transmission coefficient can be expressed as [15]

$$T = \frac{s_{11} + s_{21} - \Gamma}{1 - (s_{11} + s_{21})\Gamma}. \tag{4.4}$$

In free-space propagation, the magnetic permeability and electric permittivity can be calculated as

$$\mu_R = \frac{\lambda_0}{\Lambda}\frac{1+\Gamma}{1-\Gamma}, \qquad \varepsilon_R = \frac{\lambda_0}{\Lambda}\frac{1-\Gamma}{1+\Gamma} \tag{4.5}$$

where $\lambda_0 = c/f$ is the vacuum wavelength, and

$$\frac{1}{\Lambda^2} = -\left[\frac{1}{2\pi d}\left(\ln\left(\frac{1}{T}\right)\right) + 2j\pi n\right]^2. \tag{4.6}$$

The parameter $n = 0, \pm 1, \pm 2, \ldots$ denotes the integer of d/λ_g, where d is the thickness of the sample and $\lambda_g = \lambda_0/\sqrt{\varepsilon_R \mu_R}$ is the wavelength within the sample. As it can be observed, equation (4.6) has infinite roots due to phase ambiguity. The adequate value of n can be resolved from initial guess values of ε_R and μ_R, or by comparison of the measured and analytical values of the group delay.

In the particular situation in which μ_R is known, as in the case of non-magnetic materials for which $\mu_R = 1$, the calculation process is greatly simplified. In such a case, the electric permittivity can be directly obtained as

$$\varepsilon_R = \mu_R \frac{(1-\Gamma)^2}{(1+\Gamma)^2}. \tag{4.7}$$

which avoids the uncertainty of $1/\Lambda^2$.

In the case that $|s_{11}|$ tends to zero, as it occurs when d is a multiple of $\lambda/2$, the parameter X obtained from equation (4.3) tends to infinite, making the algorithm unstable at such frequencies. Same problem occurs with materials whose reflection coefficient is small.

4.2 NIST algorithm

In order to solve the stability problems inherent to the NRW method, a new iterative algorithm was developed by the NIST (National Institute of Standards and technology) [16]. This model serves only for ε_R determination, and it works well if a good initial guess is available. Nevertheless, it performs robustly and accurately for both low-loss and high-loss materials. Unlike NRW method, NIST algorithm provides smooth and stable results in a broadband range, as it can be observed in Fig. 4.1.

The propagation constant in free-space is defined as

$$\gamma_0 = j\frac{2\pi f}{c}, \tag{4.8}$$

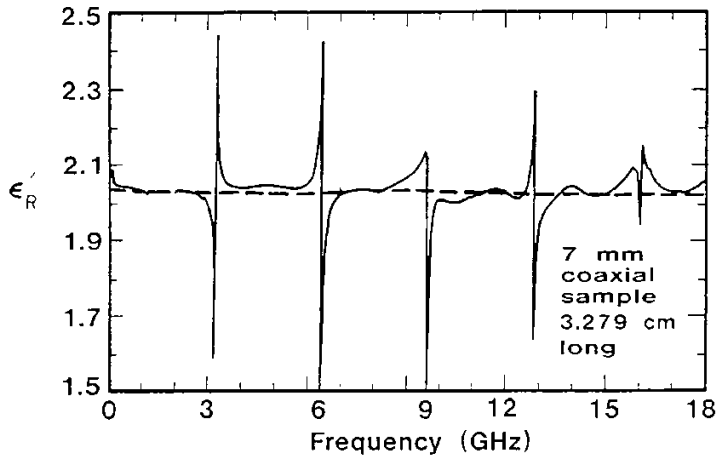

Fig. 4.1: Determination of ε_R', for a sample of Teflon with $d = 32.79$ mm, applying NRW (solid) and NIST (dashed) algorithms (source: [16]).

where c is the speed of light and f is the frequency. Within the material, the propagation constant is

$$\gamma = \frac{\gamma_0}{\sqrt{\varepsilon_R}}. \tag{4.9}$$

The reflection coefficient Γ can be calculated in terms of γ_0 and γ as

$$\Gamma = \frac{\gamma_0 - \gamma}{\gamma_0 + \gamma} \tag{4.10}$$

and the transmission coefficient T as

$$T = \exp(-\gamma d). \tag{4.11}$$

where d is the thickness of the sample.

A list of equalities is developed in [16], from which it is possible to define the following two functions

$$\begin{aligned} F_1(\varepsilon_R) &= \left| s_{11}^2 - s_{21}^2 + \frac{T^2 - \Gamma^2}{1 - \Gamma^2 T^2} \right|^2 = 0 \\ F_2(\varepsilon_R) &= \left| s_{21} - \frac{T(1 - \Gamma^2)}{1 - T^2 \Gamma^2} \right|^2 = 0. \end{aligned} \tag{4.12}$$

From an initial guess of ε_R (around ±10 % of the real value), NIST is based on estimating the roots of F_1 and F_2 by means of an iterative algorithm. In case of using the Newton method as optimization tool, the algorithm steps are as follows:

1. Assign the initial guess value $\varepsilon_R = \varepsilon_R^*$ (it can be obtained from NRW method).

2. Compute the Jacobian matrix

$$J = \begin{bmatrix} \frac{F_1(\varepsilon_R + h) - F_1(\varepsilon_R - h)}{2h} & \frac{F_1(\varepsilon_R + jh) - F_1(\varepsilon_R - jh)}{2h} \\ \frac{F_2(\varepsilon_R + h) - F_2(\varepsilon_R - h)}{2h} & \frac{F_2(\varepsilon_R + jh) - F_2(\varepsilon_R - jh)}{2h} \end{bmatrix} \tag{4.13}$$

where h is small.

3. Update a new value of ε_R as

$$\begin{bmatrix} Re\{\varepsilon_R\} \\ Im\{\varepsilon_R\} \end{bmatrix}^{new} = \begin{bmatrix} Re\{\varepsilon_R\} \\ Im\{\varepsilon_R\} \end{bmatrix} - J^{-1} \begin{bmatrix} F_1(\varepsilon_R) \\ F_2(\varepsilon_R) \end{bmatrix} \tag{4.14}$$

4. Back to step 2 until $F_1(\varepsilon_R), F_2(\varepsilon_R) < \delta$ (being δ the allowable error) or until maximum number of iterations is reached.

4.3 Other methods

4.3.1 Stable non-iterative (SNI)

This method is based on a simplified version of NRW, but corrects the instabilities for long samples using a non-iterative algorithm [17]. In the case of $\mu_R = 1$, all the steps are as described for NRW in Section 4.1 except for the final calculation of ε_R, which is obtained in this case as

$$\varepsilon_R = \frac{\lambda_0^2}{\Lambda^2}. \tag{4.15}$$

4.3.2 Transmission-epsilon-fast (TEF)

This method provides an estimation of ε_R using only the transmission parameter s_{21} [18]. It works similarly to NIST, but roots are estimated just by using function F_2 from (4.12). It works better for long samples, and is adequate for systems with significant error in the reflection measurement.

All the previously described methods are summarized in Table 4.1.

Table 4.1: Summary of the main extraction methods.

Algorithm	Measurement	Result	Best use
NRW	s_{11},s_{21}	ε_R,μ_R	Thin samples. Magnetic materials.
NIST	s_{11},s_{21}	ε_R	Thick samples. Low-loss and high-loss materials.
SNI	s_{11},s_{21}	ε_R	Thick samples. High-loss materials.
TEF	s_{21}	ε_R	Thin and thick samples. High-loss materials.

5 Experimental results

5.1 Characterization of dielectric materials

5.1.1 Teflon (5 mm)

Teflon (PTFE) is a polymer widely used as an insulating material in microwave applications, because it is chemically inert, has a high melting temperature, and is flexible and easy to machine. Its nominal dielectric properties are $\varepsilon_R \approx 2.05$ and $\tan(\delta) \sim 10^{-4}$. In this case, the measurement setup of a 5-mm thick Teflon slab in the free-space system is shown in Fig. 5.1. This sample is electrically thick, since its width is larger than the wavelength at W band (i.e., $\lambda_0 = 3$ mm at 100 GHz). The measured S-parameters (after corrections, see equation (3.2)), both in magnitude and phase, are represented in Fig. 5.2. As it can be observed, they acceptably agree with those expected from their theoretical characteristics. The dielectric constant extracted using the four methods described in Section 4 are plotted in Fig. 5.3. As it was expected, as the sample is multiple of half wavelength, the NRW method presents instabilities at the frequencies at which s_{11} tends to zero. The other three methods, NIST, SNI and TEF, provide a stable result very close to 2.05. In the case of NIST, the frequency-dependent complex electric permittivity is plotted in Fig. 5.4. The average value is $\varepsilon_R = \varepsilon_R' - j\varepsilon_R'' = 2.0406 - j0.0002$, which corresponds to $\tan(\delta) = 1.1 \cdot 10^{-4}$.

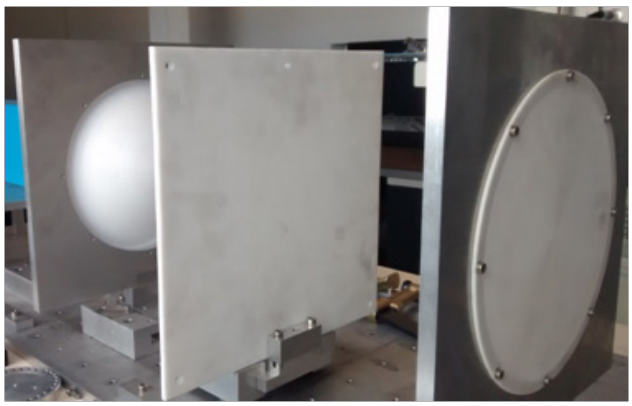

Fig. 5.1: Experimental setup for a 5-mm width sample of Teflon.

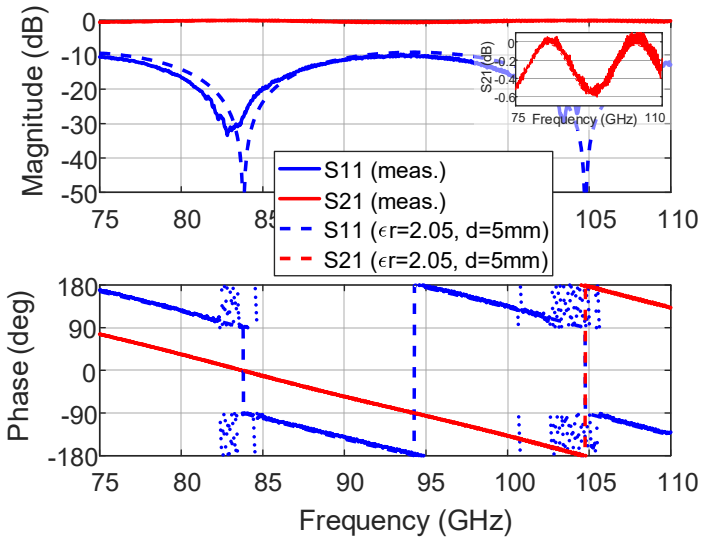

Fig. 5.2: Measured (solid) and theoretical (dashed) S-parameters of the sample of Teflon (d=5 mm).

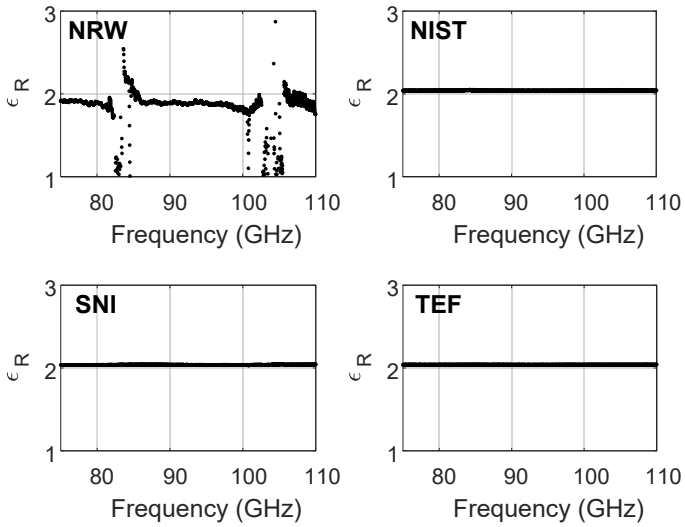

Fig. 5.3: Extracted dielectric constant of the sample of Teflon (d=5 mm) using different algorithms.

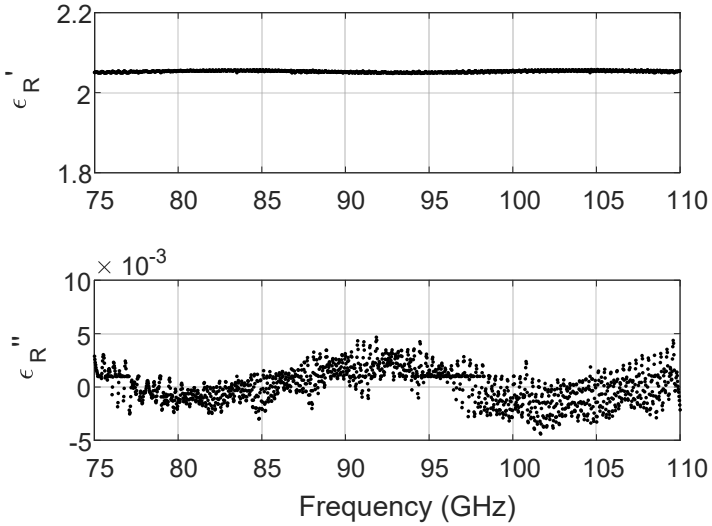

Fig. 5.4: Extracted electric permittivity of the sample of Teflon (d=5 mm) using NIST algorithm.

5.1.2 Teflon (250 µm)

In this second test, another sample of Teflon with reduced thickness (d =250 µm) has been characterized. The measured and theoretical S-parameters are plotted in Fig. 5.5. There are some discrepancies with the reflection parameter s_{11}. In this case, the sheet has been attached to an outer metallic frame. However, some practical difficulties were encountered during the experiment to hold the thin sample completely flat. If the sample does not have perfect flat and parallel faces, part of the incident power may be scattered, and consequently the reflected parameter may be undervalued. The extracted electric permittivity is presented in Fig. 5.6, and gives an average value of $\varepsilon_R = \varepsilon_R' - j\varepsilon_R'' = 1.9942 - j0.0438$. This corresponds to $\tan(\delta) = 2.2 \cdot 10^{-2}$, which is about two orders of magnitude higher than the nominal value for this material. This shows the limitations when measuring thin samples, and in particular to reliably characterize the loss tangent of materials with low losses.

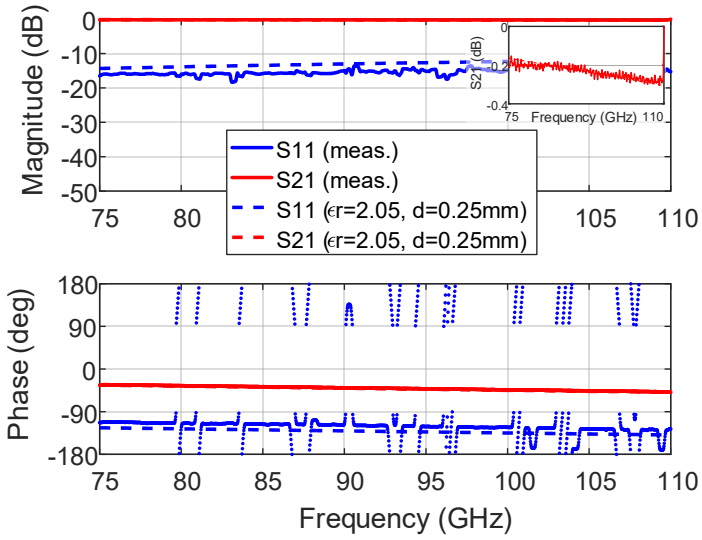

Fig. 5.5: Measured (solid) and theoretical (dashed) S-parameters of the sample of Teflon (d=250 µm).

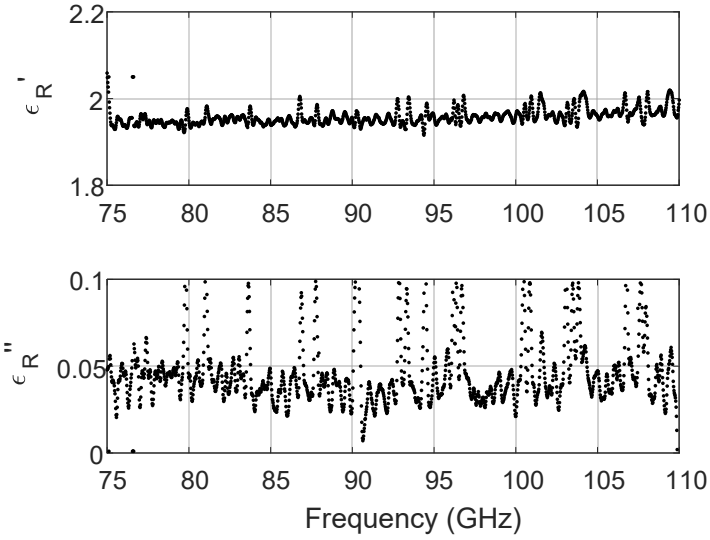

Fig. 5.6: Extracted electric permittivity of the sample of Teflon (d=250 µm) using NIST algorithm.

5.1.3 Styrofoam (30 mm)

Styrofoam (XPS) is a polymer with a dielectric constant very close to that of air, whose nominal parameters are $\varepsilon_R \approx 1.04$ and $\tan(\delta) \sim 10^{-4}$. In this case, a sample with thickness of about 29-30 mm has been measured. The experimental and theoretical S-parameters are shown in Fig. 5.7. There are some discrepancies with the magnitude of s_{11}. In any case, due to its low level, this parameter will not have much influence for the NIST algorithm (see cost functions in (4.12)). The extracted electric permittivity is represented in Fig. 5.8. The average value is $\varepsilon_R = \varepsilon_R' - j\varepsilon_R'' = 1.0337 - j0.0009$, which gives loss tangent of $\tan(\delta) = 8.4 \cdot 10^{-4}$. These values acceptably agree with those expected theoretically.

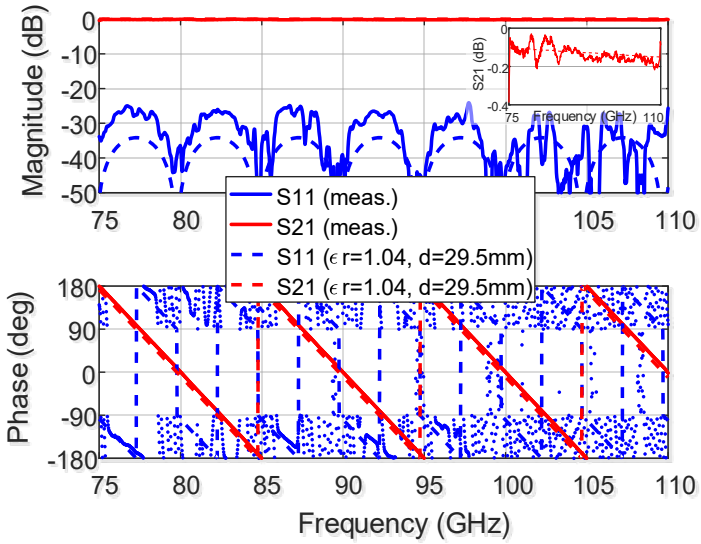

Fig. 5.7: Measured (solid) and theoretical (dashed) S-parameters of the sample of Styrofoam (d=30 mm).

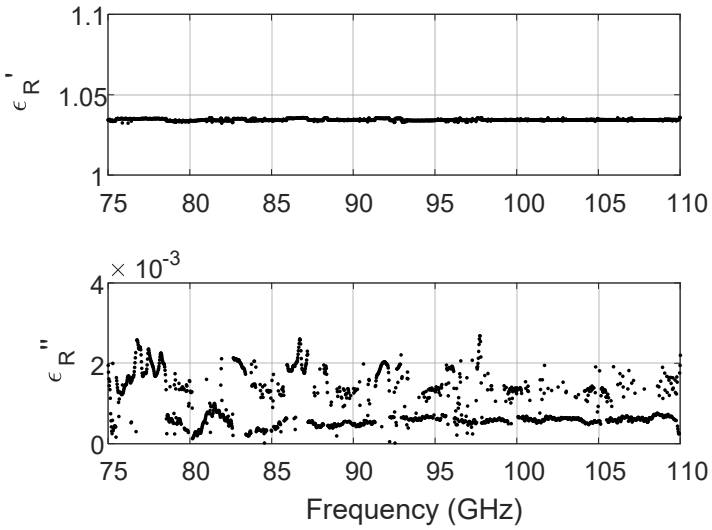

Fig. 5.8: Extracted electric permittivity of the sample of Styrofoam (d=30 mm) using NIST algorithm.

5.1.4 Kapton (75 µm)

The last dielectric sample is a very thin sheet of Kapton (PI) of $d = 75$ µm. The nominal dielectric parameters are $\varepsilon_R \approx 3.4$ and $\tan(\delta) \sim 10^{-2}$. The measured and theoretical S-parameters are shown in Fig. 5.9. The experimental results reproduce well the predicted response, although some instabilities appear in the lower part of the band. The calculated electric permittivity is presented in Fig. 5.10. The average value is $\varepsilon_R = \varepsilon_R' - j\varepsilon_R'' = 3.2174 - j0.0483$, and the corresponding loss tangent is $\tan(\delta) = 1.5 \cdot 10^{-2}$, which reasonably agree with the nominal parameters.

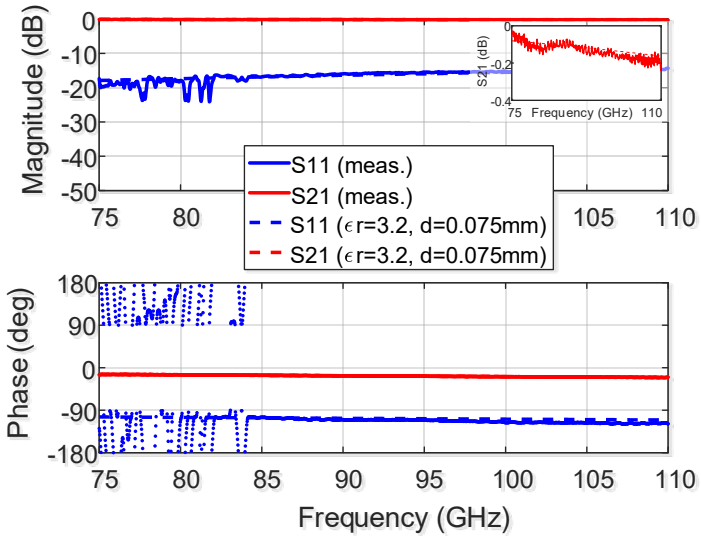

Fig. 5.9: Measured (solid) and theoretical (dashed) S-parameters of the sample of Kapton (d=75 µm).

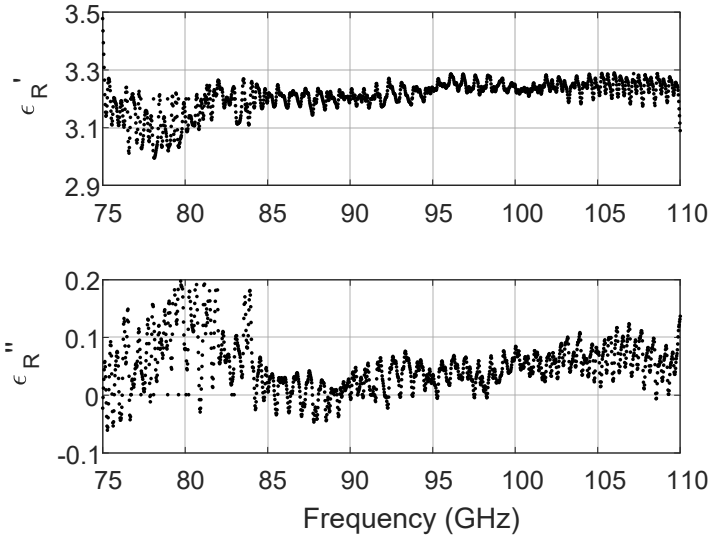

Fig. 5.10: Extracted electric permittivity of the sample of Kapton (d=75 µm) using NIST algorithm.

5.1.5 Summary of results

The extracted dielectric parameters obtained from the different material samples are summarized in Table 5.1. In view of the results, some conclusions can be drawn:

- Thicker samples are preferable for more accurate results.
- In the experiments, regardless the sample thickness, the extracted dielectric constant acceptably agreed with the nominal values (<5.5% error).
- In the case of low-loss materials (e.g., Teflon or Styrofoam), the sample thickness should be in the order the wavelength (i.e., 3 mm at 100 GHz) to get reliable values of the loss tangent.
- In the case of 'lossy' materials, such as Kapton, the obtained loss tangent value was in the order of magnitude of the nominal value, despite the extremely thin sheet used for the test.

Table 5.1: Extracted parameters for a set of dielectric samples.

Sample	$\boldsymbol{\varepsilon'_R}$		$\boldsymbol{\tan(\delta)}$	
(material, thickness)	**Nom.**	**Meas.**	**Nom.**	**Meas.**
Teflon (PTFE), 5 mm	2.05	2.0406	~10^{-4}	$1.1{\cdot}10^{-4}$
Teflon (PTFE), 250 µm	2.05	1.9942	~10^{-4}	$2.2{\cdot}10^{-2}$
Styrofoam (XPS), 30 mm	1.04	1.0337	~10^{-4}	$8.4{\cdot}10^{-4}$
Kapton (PI), 75 µm	3.4	3.2174	~10^{-2}	$1.5{\cdot}10^{-2}$

5.2 Measurement of quasioptical components

Apart from the characterization of dielectric materials, the implemented measurement system also serves to obtain the free-space reflection/transmission parameters of any quasioptical device, including matching layers, corrugated slabs, absorbers, frequency selective surfaces or polarizers. Two examples will be presented below: a pyramid-array matched load, and a wire-grid polarizer.

5.2.1 Matched load

The matched load is made of *Eccosorb* MF-117, is based on a pyramidal array structure, and its diameter is 90 mm. The experimental setup, which is shown in Fig. 5.11, requires one half of the measurement system, since only the reflection coefficient is measured. Accordingly, it is necessary to establish a 1-port calibration procedure. In this respect, three standards are used for this test: short, λ/4-offset short, and match (see Fig. 5.12). Since the size of the load is comparable to that of the beam-waist, the sample has been surrounded by microwave absorber to avoid stationary waves due to secondary lobes. This absorbing foam is also present during calibration, so that its effect is eliminated from the measurements.

The obtained reflection coefficient (s_{11}) is represented in Fig. 5.13. It has been tested for two load orientations: electric field parallel to the grid described by the pyramids ($\phi = 0$), and rotated 45 degrees ($\phi = 45º$). It can be observed how the reflection parameter is unaffected by the relative orientation between the radiated field and the load. The return losses are better than -23 dB in the whole band of interest.

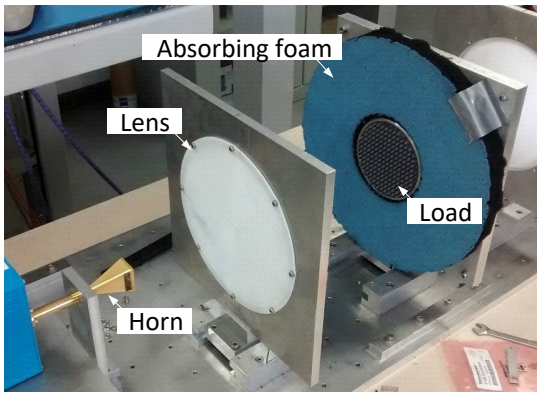

Fig. 5.11: Measurement setup for the pyramid-array matched load.

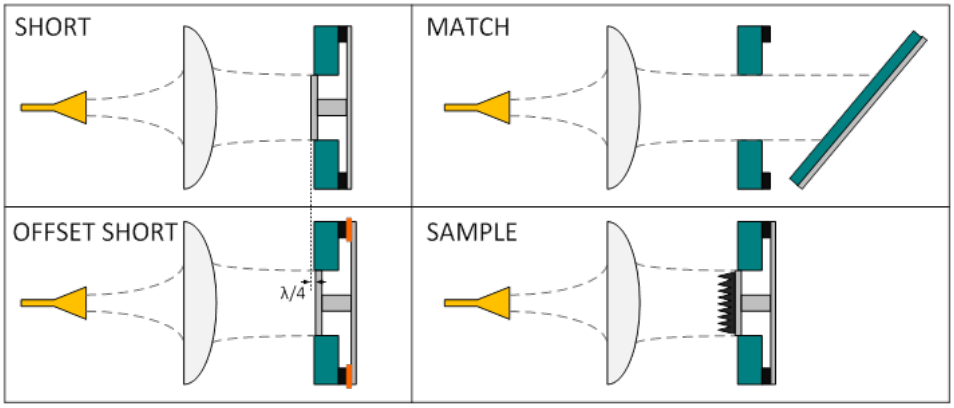

Fig. 5.12: One-port calibration procedure for the matched load, based on short, offset-short and match standards.

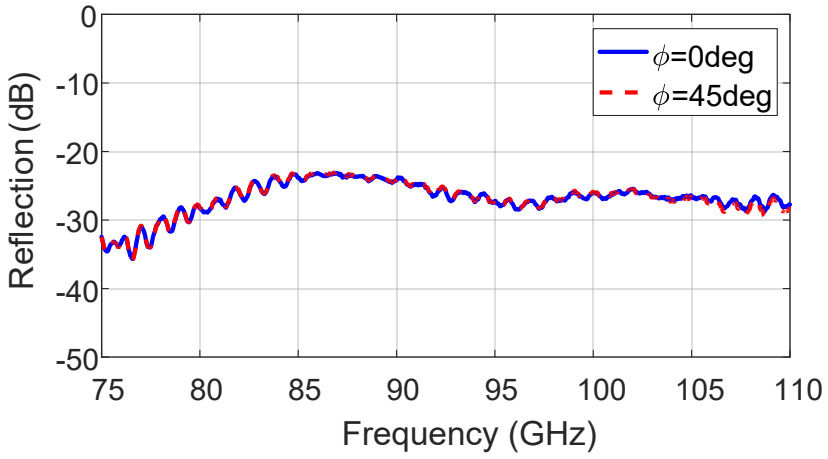

Fig. 5.13: Measured reflection coefficient of the pyramid-array matched load.

5.2.2 Wire-grid polarizer

Grid polarizers consist of many thin parallel metallic wires placed in a plane, and are utilized as beam splitters/diplexers, variable attenuators or reflectors [8]. The measurement setup for the characterization of a wire grid is shown in Fig. 5.14. During the calibration and measurement, the metallic frame around the window of the grid polarizer has been covered with absorbing material to avoid undesired reflections on the metallic surface. In this case, a full 2-port TRM calibration is performed.

The measured transmission for different orientations of the grid polarizer is shown in Fig. 5.15. When the electric field is oriented parallel to the wires, the grid behaves as a metallic surface, and the incident wave ($E_{\parallel}$) has to be reflected. In this case, the measured isolation is better than -32 dB. When the electric field is perpendicular to the wires, the incident wave ($E_{\perp}$) is able to pass through the grid. The measured insertion loss in this second scenario is about -0.25 dB. Finally, when the grid is oriented at 45º, the incident field ($E_{45º}$) can be decomposed in two components, parallel and perpendicular to the wires respectively. Consequently, only one half of the power –associated to the perpendicular component– passes through the grid. The transmission parameter is about -6 dB in this last case. The additional -3 dB factor is due to polarization mismatch at the receiving antenna.

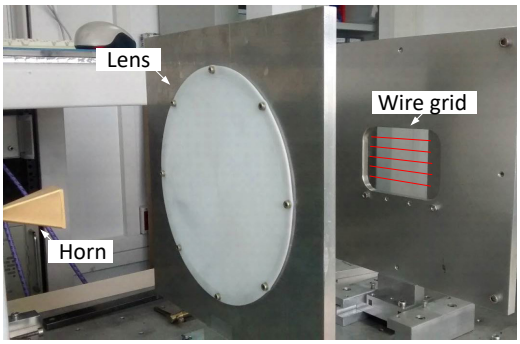

Fig. 5.14: Measurement setup for the wire grid polarizer (red lines indicate the orientation of the wires).

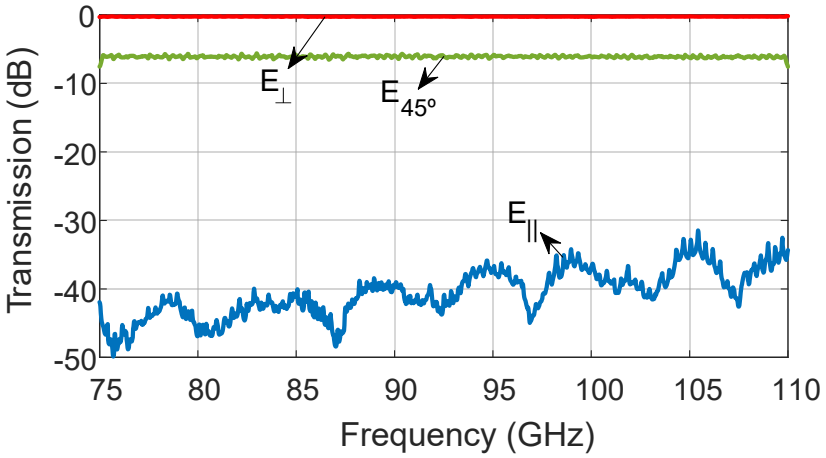

Fig. 5.15: Measured transmission of the wire-grid polarizer for different orientations of the incident electric field relative to the wires.

6 Conclusion

Free-space measurement systems allow the experimental validation of microwave and millimeter-wave components, and is particularly useful in the field of radio astronomy systems. In this work, a free-space setup working at W-band (75-110 GHz) has been presented. The quasioptical theory has been demonstrated to be a simple but powerful tool to predict the optical characteristics and performance of the system. The implemented setup has been successfully validated by multiple experimental results, including the electrical characterization of dielectric materials and mm-wave components. In the near future, we plan to extend the functionality of the system to cover also the Q-band (33-50 GHz).

References

[1] Keysight Technologies, “Basics of measuring the dielectric properties of materials”, *Appl. Note 5989-2589EN*, Apr. 2015.

[2] T. P. Marsland, S. Evans, “Dielectric measurements with an open-ended coaxial probe”, *IEE Proceedings*, vol. 134, no. 4, pp. 341-349, Aug. 1987.

[3] A. M. Nicolson, G. F. Ross, “Measurement of the intrinsic properties of materials by time-domain techniques”, *IEEE Trans. Instrum. Meas.*, vol. 19, no. 4, pp. 377-382, Nov. 1970.

[4] A. Parkash, J. K. Vaid, A. Mansingh, “Measurement of dielectric parameters at microwave frequencies by cavity-perturbation technique”, *IEEE Trans. Microw. Theory Tech.*, vol. 27, no. 9, pp. 791-795, Sep 1979.

[5] D. K. Ghodgaonkar, V. V. Varadan, V. K. Varadan, “Free-space measurement of complex permittivity and complex permeability of magnetic materials at microwave frequencies”, *IEEE Trans. Instrum. Meas.*, vol. 39, no. 2, pp. 387-394, Apr. 1990.

[6] P. F. Goldsmith, *Quasioptical systems*. IEEE Press, 1998.

[7] J. W. Goodman, *Introduction to Fourier optics*. Roberts & Company, 3rd ed., 2005.

[8] E. Hecht, *Optics*. Pearson, 5th ed., 2017.

[9] T. Morita, S. B. Cohn, “Microwave lens matching by simulated quarter-wave transformers”, *IRE Trans. Antennas Propag.*, vol. 4, no. 1, pp. 33-39, Jan. 1956.

[10] T. K. Gaylord, W. E. Baird, M. G. Moharam, “Zero-reflectivity high spatial-frequency rectangular-groove dielectric surface-relief gratings”, *Appl. Opt.*, vol. 25, no. 4, pp. 4562-4567, Dec. 1986.

[11] Keysight Technologies, “PNA microwave network analyzers”, *Appl. Note 5989-4098EN*, Aug. 2014.

[12] P. G. Bartley, S. B. Begley, “Improved free-space S-Parameter calibration”, *Instrum. Meas. Tech. Conf.*, May 2005.

[13] Keysight Technologies, “Questions about free space GRL calibration”, *Discussion Forums*, Nov. 2006.

[14] N. Gagnon, J. Shaker, L. Roy, A. Petosa, P. Berini, “Low-cost free-space measurement of dielectric constant at Ka band”, *IEEE Proc.-Microw. Antennas Propag.*, vol. 151, no. 3, Jun. 2004.

[15] W. B. Weir, “Automatic measurement of complex dielectric constant and permeability at microwave frequencies”, *Proc. IEEE*, vol. 62, no. 1, pp. 33-36, Jan. 1974.

[16] J. Baker-Jarvis, “Transmission/reflection and short-circuit line permittivity measurements”, *NIST Technical Note 1341*, Jul. 1990.

[17] A. H. Boughriet, C. Legrand, A. Chapoton, “Noniterative stable transmission/ reflection method for low-loss material complex permittivity determination”, *IEEE Trans. Microwave Theory Tech.*, vol. 45, no. 1, pp. 52-57, Jan. 1997.

[18] Keysight Technologies, “Materials measurement suite”, *Tech. Overview 5992-0263EN*, Mar. 2016.